COMPUTERS IN BIOLOGY AND MEDICINE

https://www.journals.elsevier.com/computers-in-biology-and-medicine/editorial-board/edward-ciaccio-phd

Editor in Chief: Prof. Dr. Edward Ciaccio, Columbia University, New York, USA.

Impact Factor: 3.434; ISSN: 0010-4825

(ACCEPTED SEPTEMBER 28TH 2020)

MICROPOLAR PULSATILE BLOOD FLOW CONVEYING NANOPARTICLES IN A STENOTIC TAPERED ARTERY: *NON-NEWTONIAN PHARMACODYNAMIC SIMULATION*

B. Vasu[a] *, Ankita Dubey[a], O. Anwar Bég[b] *and* Rama Subba Reddy Gorla [c]

*[a]Department of Mathematics, Motilal Nehru National Institute of Technology Allahabad, Prayagraj, Uttar Pradesh- 211004, **India**.*
**Corresponding author- email:* bvasu@mnnit.ac.in
*[b]Professor of Engineering Scence, Dept. of Mechanical and Aeronautical Engineering, School of Science, Engineering and Environment (SEE), Newton Building, Salford University, Manchester, M54WT, **UK**. **E:** O.A.Beg@salford.ac.uk*
*[c]Professor, Department of Aeronautics and Astronautics, Air Force Institute of Technology, Wright Patterson Air Force Base, Dayton, Ohio 45433, **USA. E:** r.gorla@yahoo.com*

ABSTRACT

Two-dimensional rheological laminar hemodynamics through a diseased tapered artery with a mild stenosis present is simulated theoretically and computationally. The effect of different metallic nanoparticles homogeneously suspended in the blood is considered, motivated by drug delivery (pharmacology) applications. The Eringen micropolar model has been deployed for hemorheological characteristics in the whole arterial region. The conservation equations for mass, linear momentum, angular momentum (micro-rotation), and energy and nanoparticle species are normalized by employing suitable non-dimensional variables. The transformed equations are solved numerically subject to physically appropriate boundary conditions using the finite element method with the variational formulation scheme available in the FreeFEM++ code. A good correlation is achieved between the FreeFEM++ computations and existing results. The effect of selected parameters (taper angle, Prandtl number, Womersley parameter, pulsatile constants, and volumetric concentration) on velocity, temperature, and micro-rotational (Eringen angular) velocity has been calculated for a stenosed arterial segment. Wall shear stress, volumetric flow rate, and hemodynamic impedance of blood flow are also computed. Colour contours and graphs are employed to visualize the simulated blood flow characteristics. It is observed that by increasing Prandtl number (*Pr*), the micro-rotational velocity decreases i.e., microelement (blood cell) spin is suppressed. Wall shear stress decreases with the increment in pulsatile parameters (B *and e*), whereas linear velocity increases with a decrement in these parameters. Furthermore, the velocity decreases in the tapered region with elevation in the Womersley parameter (α). The simulations are relevant to transport phenomena in pharmacology and nano-drug targeted delivery in hematology.

KEYWORDS: *Nano-pharmacodynamics; Tapered artery; Hemo-rheology; Micropolar fluid model; Nano-drugs; Pressure gradient; Wall shear stress; hemodynamic impedance; Finite Element Method, FreeFEM++.*

1. INTRODUCTION

The mechanics of blood flow is fundamental to the formation and evolution of cardiovascular diseases. As elaborated by Skalak *et al.* [1], this subject has been evolved significantly over centuries. The sophisticated multi-physical simulations have become practical in hemodynamic simulation, featuring transport in complex geometries (bifurcations, bends, constrictions, etc.)

and rheological characteristics computation. In the last few decades, a significant progress can be seen in the combination of more sophisticated fluid dynamics models and numerical procedures to improve the analysis of real blood flows [2]. This has aided extensive improvement in our understanding of the multiple causes, progression, and possible treatments for various haematological conditions and diseases [3]. The blood flow characteristics in an artery can be changed significantly by arterial disease and common conditions which are aneurysms (vessel bulge) and stenoses (vessel constriction). The progress of atherosclerosis or stenosis in a blood vessel induced by the addition of lipids in the arterial wall is absolutely common. The growth of atherosclerotic plaques that bulge into the lumen, resulting in stenosed blood vessels and one of the most severe consequences of this obstruction can be count as resistance increment and the concomitant reduction of the blood flow to the specific vascular bed.

Over the past few decades, an impressive number of comprehensive theoretical and experimental investigations related to blood flow in arteries in the presence of stenosis has been conducted with various methodologies [4]. Padma *et al.* [5], presented a mathematical model for blood flow in a diseased mild stenotic artery. The numerical simulations [6-9] of arterial blood flow have also assumed great importance due to their wide range of clinical applications and have utilized many different computational methods, including finite differences, finite elements, immersed boundary methods, finite volume solvers, molecular dynamics and smoothed particle hydrodynamics (SPH). These studies are fundamental to the human circulatory system [10].

Bio-rheological hemodynamics has therefore emerged as a major branch of modern medical fluid mechanics. In recent years an increasing focus has been devoted to exploring real blood flows with a diverse spectrum of non-Newtonian models [11-15]. Cokelet [16] provided a seminal review of various rheological models for human blood. Shibeshi and Collins [17] presented the general classification of non-Newtonian models on blood flow simulations to various degrees of accuracy. Amiri *et al.* [18] used a commercial numerical package (ANSYS FLUENT) to simulate an unsteady 3-D non-Newtonian (Carreau shear-thinning) flow in the femoral blood artery using fluid-structure interaction. The model is considered as real model extraction of computerized tomography (CT) scan images of an artery bifurcation with moderate arteriosclerosis. Jamalabadi *et al.* [19] used a finite volume algorithm to numerically simulate the electrically conducting unsteady blood flow of Carreau-Yasuda fluid in the presence of a transverse magnetic field, noting that a flow pressure drop occurs for blockages

of more than 60 percent. Shabbir *et al*. [20] considered the transient Herschel–Bulkley hemodynamics in a diseased artery in the presence of multi-irregular stenoses using perturbation and Newton-Raphson iterative techniques. Ponalagusamy and Manchi [21] have investigated the blood flow through a stenotic artery in the four-layered model comprises a cell-rich core of suspension of all the erythrocytes described as a non-Newtonian (Jeffrey) fluid, a peripheral zone of cell-free plasma (Newtonian fluid) and the stenosed artery with a porous wall consisting of a thin transition (Brinkman) layer followed by a Darcy porous region. They observed that higher hematocrit (volume percentage of red blood cells in plasma) elevates both hemodynamic impedance and wall shear stress (WSS) whereas the converse response is induced with greater plasma layer thickness, Jeffrey viscoelastic parameter, Darcy number, and Darcy slip parameter.

Several theoretical studies related to *rheological blood flow through stenotic arteries* have also appeared in recent years. Tzirakisa *et al*. [22] studied the Hershel–Bulkley biomagnetic blood flow model in a duct using a discontinuous/continuous Galerkin algorithm with a symmetric weighted interior penalty (SWIP) formulation and a Hershel–Bulkley model. They noted significant deviations in flow symmetry and wall shear stress from the Newtonian fluid model, for the case of a straight, rigid vessel with a 60% axisymmetric stenosis. Popular, although simplistic models deployed in this context, include viscoplastic [23] and power-law [24] models. Mekheimer and El kot [25], have discussed the time dependent blood flow with Sisko viscoelastic rheology in an overlapping anisotropic tapered stenotic elastic artery numerically. The above studies did not consider *micro-structural* effects in blood. Conventional non-Newtonian models such as viscoelastic, viscoplastic, generally modify the Newtonian model with supplementary stress tensors. They cannot simulate microscopic rotational motions (gyration of fluid micro-elements), which characterize suspensions in blood e.g., erythrocytes, leukocytes, proteins, fats, etc. In a groundbreaking study, Eringen [26] introduced the *micropolar fluid* model for viscous fluent media containing suspensions through classical continuum and thermodynamics laws incorporating new kinematic variables (gyration tensor, micro-inertia moment tensor) and concepts of body moments, stress moments and micro-stresses. The Eringen micromorphic formulation provides a much more sophisticated framework for simulating actual microrheological properties of biofluids, including blood, synovial fluid, gastric liquids, lymph, semi-circular canal fluid, etc. Eringen [27] generalized the micropolar model to microstretch fluids and further presented a rigorous appraisal of modifications of this theory in [28]. Over the past five decades, micropolar theory has therefore been implemented successfully in diverse branches of medical fluid dynamics. Ariman [29]

presented the first study of micropolar and microstretch blood flows in his analysis of small arteries of 100 micro meter diameters, deriving extensive analytical solutions for velocity, micro-rotation velocity, and microstretch to simulate deformable substructures in the blood (flexibility of erythrocytes) in addition to the independent spin of red cells under no-slip conditions at the vessel walls. A seminal investigation into micropolar blood flows was subsequently presented by Kang and Eringen [30] who, via energy considerations, developed new relationships for microelement concentration and gyration involving both macro- and micro motions in vessel hemodynamics. The micropolar model therefore provides a more realistic model for bio-fluid rheology [31, 32] compared with simpler polar models [33] which only include couple stress effects and therefore provide no field variable to simulate the variation of local hematocrit with radial position in actual blood flows. Subsequently, many researchers have explored the micropolar model in biofluid mechanics. Interesting areas investigated with this theory include drag effects on individual erythrocytes in Stokesian flows [34], capillary blood flows [35], biomagnetic hemodynamics in vascular tissue [36], deoxygenated hemodynamics [37], biotribology [38, 39], gastric transport phenomena [40], flow in trabecular bone [41], bacterial hydrodynamics [42], biomembranes [43], electrokinetic bio-microfluidics [44], biomaterial filtration [45] and ciliated propulsion in respiration [46]. Some interesting analyses in stenotic hemodynamics have also considered the micropolar rheological model, including Devanathan and Parvathamma [47] on single stenosed arteries. Mass diffusion in micropolar stenotic tapered arterial blood flows has been addressed by Mekheimer and El Kot [48], Ikbal *et al.* [49] and Samad [50]. Ellahi *et al.* [51] computed arterial micropolar blood flow through a composite mild stenotic arterial segment. Zaman *et al.* [52] used a forward time centered space (FTCS) finite difference code to simulate transient micropolar blood flow in a catheterized stenotic arterial annular geometry. Very recently, Tiwari *et al.* [53] analyzed the hemodynamics in stenosed porous layered micro-vessels using both Eringen micropolar and Newtonian fluid models. All these studies have confirmed the superior abilities of micropolar theory in analysing practical hemodynamic transport problems.

Significant progress in *nanoscale biomechanics and simulation* has also rapidly accelerated the production of more functional advanced nanomaterials and mobilized numerous pathways for advancing medical science, pharmacology, tissue repair, ocular medications, and the treatment of many diseases to achieve maximal therapeutic efficacy with minimal side effects. Sahoo *et al.* [54] explored the potential clinical applications of nanotechnology in medical sciences with scientific and technical aspects. Blood mediated nanoparticle transport achieves impressive

results in enhancing the heat and mass diffusion properties of drugs, i.e., pharmacological agents injected into the blood vessel. The use of nano- carriers formulated with dendrimers, liposomes, micelles, solid lipid nanoparticles, and gold, silver, and titanium oxide and cadmium sulphide polymeric nanoparticles together with magnetic nanoparticles have been shown to substantially improve the efficacy of conventional pharmacological agents [55]. In hemodynamic therapies, the base liquid is blood and can be doped with a variety of biocompatible nanoparticles, including gold. Bio-nanomedicine enhances the solubility, bioavailability, absorption, targeting, and controlled release of drugs [56, 57]. Akbar *et al.* [58] simulated nano-pharmacodynamic transport in unsteady variable viscosity blood flow through an overlapping stenotic artery with wall mass transfer and hydrodynamic slip effects. A theoretical analysis of blood mediated nanoparticle transport to combat the arterial disease was presented by Ijaz and Nadeem [59]. Tripathi and Bég [60] considered thermosolutal buoyancy effects in nano-doped hemodynamics in a two-dimensional channel with long wavelength and low Reynolds number approximations. Vasu *et al*. [61] presented extensive finite element simulations and contour visualizations using the FreeFEM++ code of the axisymmetric electro-conductive viscoelastic nano-doped hemodynamics in a stenosed coronary artery with rigid walls under the radial magnetic field. They found that considerable acceleration is induced with increasing Brownian motion parameter and that a narrower stenosis significantly alters the temperature and nano-particle distributions and flow structures. An analytical solution for the hemodynamic study of gold nanoparticles in blood flow through tapered stenosis was reported by Elnaqeeb *et al.* [62] under the mild stenosis assumption. They studied different nanoparticles, such as Au, Cu, TiO_2, and observed that gold nanoparticles achieve the most notable enhancement in blood flow and hemodynamic performance in the diseased artery. Very recently, Dubey *et al.* [63] investigated the effect of metallic nanoparticles on the blood flow through a diseased artery with hemorheological characteristics. Zaman *et al.* [64] employed a hybrid nanofluid model to simulate unsteady laminar hemodynamic flow through the stenosed tapered artery (converging and diverging) with an aneurysm and rigid walls, noting that hybrid Ag-Al_2O_3 nano-particles within blood induce significant deceleration compared with only homogenous silver nanoparticles (Ag).

The above studies *did not simultaneously consider both microstructural fluid rheology and nanoscale effects*. A possible methodology for simulating nanoparticle behavior and microstructural hydrodynamics is the combination of Eringen micropolar and nanofluid models. Although very limited attention has been devoted to hemodynamics, several robust mathematical models of *micropolar nanofluid dynamics in bioengineering* have been

communicated. Prasad *et al.* [65] used the Keller box second-order finite difference scheme and a combined micropolar Buongiorno nanofluid model to compute the enrobing flow of bio-nanopolymers on cylindrical components. Latiff *et al.* [66] used MAPLE quadrature to simulate the time-dependent microorganism-doped bioconvection nanofluid flow from contracting and extending coatings for anti-fouling applications. Computational pharmacodynamics plays a vital role in understanding drug delivery processes, the development of direct drug delivery methods with associated devices, and evaluation of drug delivery efficiency. It can be used to model aerosol dynamics in the human respiratory systems and particle hemodynamics in the human vasculatures and tissue heat and mass transfer as aspects of pharmacokinetics. Such capabilities with fairly realistic and accurate results at relatively low costs make computational pharmacodynamics a perfect tool for research and development in drug delivery. Numerous mathematical studies have explored the influence of bio-nanofluid transport in biomedical applications; however, these simulations have ignored micro-rotational effects. Motivated by presenting a more general *microstructural fluid dynamics framework for nano-pharmacodynamics in blood flows*, in the present article, a detailed finite element study is conducted of unsteady micropolar nano-doped hemodynamics, heat and mass transfer in a tapered diseased stenotic artery. Eringen's non-Newtonian micropolar theory is deployed to mimic rotary motion (gyration) of micro-fluid elements in the blood. A modified Tiwari-Das homogenous nanoscale model [67] is deployed to study specific metallic nanoparticle dynamics. The versatile FREEFEM++ finite element software [68] is employed to solve the nonlinear conservation equations. These aspects constitute the novelties of the present work. Extensive finite element simulations are conducted with physically realistic material properties and boundary conditions and graphical visualization of the impact of micromorphic, nanoscale, thermophysical and geometric parameters on velocity, temperature and micro-rotational (Eringen angular) velocity, wall shear stress (WSS), volumetric flow rate and hemodynamic impedance of blood flow. Detailed interpretation of the computations is also provided of direct relevance to pharmacological nanoparticle-mediated rheological blood flow in stenotic arterial systems.

2. MATHEMATICAL MODELLING OF BIORHEOLOGICAL NANO-DOPED FLOW

Unsteady two-dimensional laminar blood flow in a tapered artery is considered wherein blood flow is modelled as a homogeneous fluid containing randomly distributed suspensions. Blood rheology is simulated with the micropolar fluid model. Heat and mass transfer are also present. Gold (Au) nanoparticles are injected into micropolar blood flowing through a stenotic tapered

artery. For the simulations, the pulsatile nature of blood has also been included. The velocity is taken as zero at the walls of the vessel, i.e., no-slip. We have considered a mild stenosis i.e. the level of stenosis is 40% in the diverging tapering artery, 60% in converging tapering artery and a little more than 50% in the non-tapered artery respectively. A cylindrical coordinate system (r,θ,z) is therefore adopted where the flow in the θ-direction has been neglected, i.e., the flow is only in the radial (i.e., r-axis) and axial (z-axis) directions as shown in **Fig. (1).** The fluid is incompressible. The tapered stenotic artery has finite length L and contains a symmetric stenosis with maximum depth δ and length J_1. The geometry of the stenosis which is assumed to be symmetric can be described using the following relations:

$$\begin{aligned} \bar{R}(\bar{z}) &= \bar{h}(\bar{z})\left[1-\eta\left(J_1^{\,n-1}(\bar{z}-J_0)-(\bar{z}-J_0)^n\right)\right] && J_0 \le \bar{z} \le J_0+J_1 \\ &= \bar{h}(\bar{z}) && otherwise \end{aligned} \tag{1}$$

$$\bar{h}(\bar{z}) = d_0 + \zeta \bar{z} \tag{2}$$

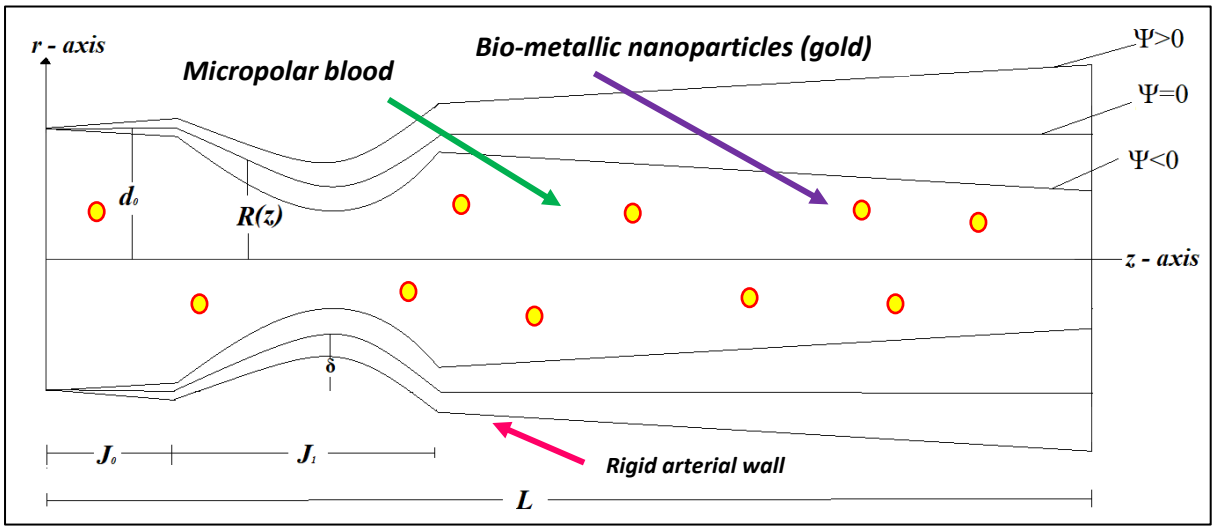

Figure 1. Schematic for micropolar nano-doped stenosed tapered arterial hemodynamics

Here $h(z)$ is the radius of the tapered arterial segment in the stenotic region, d_0 is the radius of the non-tapered artery in the non-stenotic region, ξ is the tapering parameter, J_1 is the length of the stenosis, $n(>2)$ is a parameter determining the shape of the constriction profile which is termed the *shape parameter* and J_0 indicates its location (as shown in Fig. 1). The parameter η in Eqn. (1) s given by:

$$\eta = \frac{\delta}{d_0 J_1^{\,n}} \frac{n^{\frac{n}{n-1}}}{n-1} \tag{3}$$

Here δ represents the maximum height of the stenosis located at $z = J_0 + \frac{J_1}{\frac{1}{n^{n-1}}}$.

2.1 ***Physical properties of nanoparticles***

Blood is a suspension of tiny particles in a complex, continuous, aqueous solution, called plasma. The tiny particles defined as cells consist of a variety of blood cells, e.g., erythrocytes (red blood cells i.e., RBCs), leukocytes (white blood cells), lipoproteins, and platelets. In blood, RBCs occupy about 97% of the total cell volume, and their shape, size, deformation, and flexibility play a critical role in blood rheology. The physical properties such as specific heat capacity and thermal expansion coefficients dependent on density and temperature of the micropolar fluid based on Tiwari-Das nanoparticle volume fraction relations [67] are defined as:

$$\rho_{nf} = \rho_f(1-\phi) + \rho_s\phi \tag{4}$$

$$(\rho c_p)_{nf} = (\rho c_p)_f(1-\phi) + (\rho c_p)_s\phi \tag{5}$$

$$\frac{K_{nf}}{K_f} = \frac{\left(K_s + 2K_f\right) - 2\phi\left(K_s - K_f\right)}{\left(K_s + 2K_f\right) + \phi\left(K_s - K_f\right)} \tag{6}$$

The nanoparticles are uniformly dispersed and are stable in the base fluid (blood). As noted in [67], among many other studies, the relative change in the concentration of the nanoparticles with respect to the base fluid is parabolic. The nanofluid's viscosity is a function of the volume fraction of the nanoparticles in the base fluid. This methodology pre-dates modern nanofluid sciences. In the early 20th century, Einstein derived a famous equation using his Brownian motion theory, by studying the effect on the motion of a liquid containing very small spheres, suspended inside the liquid. Einstein's relation is valid for the low volume fraction of the suspended spheres and represented as:

$$\mu_{nf} = \mu_f(1 + 2.5\phi) \tag{7}$$

The classical Brinkman model developed much later -see Happel and Brenner [69] applies to the viscosity of concentrated suspensions and solutions and takes the form:

$$\mu_{nf} = \frac{\mu_f}{(1-\phi)^{2.5}} \tag{8}$$

Batchelor [70] also considered the bulk stress, which appears owing to the Brownian motion in the dilute case, where the effective viscosity is considered as:

$$\mu_{nf} = \mu_f (1 + 2.5\phi + 6.2\phi^2) \tag{9}$$

All these models are classical and may be used appropriately for numerical simulations. However, they are not completely adequate for all types of nanofluids. Many researchers have verified the correct viscosity formulation for different nanoparticles through experiments, e.g., [67]. In the present study, the relations for the ratio of nanofluid viscosity (i.e. nano-doped blood) to the base fluid viscosity (blood) μ_{nf}/μ_f are used as given in **Table 1.** The present simulations investigate the variations in the flow characteristics due to the doping of blood with Gold (*Au*) nano-particles, Copper (*Cu*) nanoparticles, Titanium Oxide (TiO_2) and Aluminium Oxide (Al_2O_3) nanoparticles (other properties e.g. density are also given in **Table 1**).

Table 1. Thermo-physical properties of blood and different metallic nanoparticles

	Gold (Au)	**Copper (Cu)**	**Titanium (TiO_2)**	**Alumina (Al_2O_3)**	**Blood**
$\rho(Kg/m^3)$	19320	8933	4250	3970	1063
$c_p(J/Kg\,K)$	1288	235	686.2	765	3594
$K(W/m\,K)$	314.4	401	8.9538	40	0.492
$\gamma\times10^{-5}(K^{-1})$	1.4	1.67	1.9	0.85	0.18
μ_{nf}/μ_f	$\frac{1}{(1-\phi)^{2.5}}$	$\frac{1}{(1-\phi)^{2.5}}$	$\frac{1}{(1-\phi)^{2.5}}$	$\frac{1}{(1-\phi)^{2.5}}$	

2.2 ***Governing Equations***

Here *u* and *w* are the velocity components in the *r* and *z* directions. Neglecting body forces, the governing equations for the hemodynamic transport may be presented in vectorial form as:

$$\nabla\cdot\bar{V} = 0 \tag{11}$$

$$\rho_{nf}\left(\frac{\partial\bar{V}}{\partial\bar{t}} + \bar{V}\cdot\nabla\bar{V}\right) = -\nabla\bar{p} + k\nabla\times\bar{V} + (\mu_{nf} + k)\nabla^2\bar{V} \tag{12}$$

$$\rho_{nf} J\left(\frac{\partial\bar{N}}{\partial\bar{t}} + \bar{V}\cdot\nabla\bar{N}\right) = -2k\bar{N} + k\nabla\times\bar{V} + \gamma(\nabla\times\nabla\times\bar{N}) + (\alpha' + \beta + \gamma)\nabla(\nabla\cdot\bar{N}) \tag{13}$$

$$(\rho c_p)_{nf}\left(\frac{\partial\bar{T}}{\partial\bar{t}} + \bar{V}\cdot\nabla\bar{T}\right) = K_{nf}\nabla^2\bar{T} \tag{14}$$

Further, the micropolar material constants μ_{nf}, $k, \alpha^{'}, \beta$ and γ satisfy the following inequalities $2\mu_{nf} + k \geq 0,\ k \geq 0,\ 3\alpha^{'} + \beta + \gamma \geq 0$ *and* $\gamma \geq |\beta|$.

Since the flow is axisymmetric, the governing equations can be reduced to:

$$\frac{\partial \bar{u}}{\partial \bar{r}} + \frac{\bar{u}}{\bar{r}} + \frac{\partial \bar{w}}{\partial \bar{z}} = 0 \tag{15}$$

$$\rho_{nf}\left(\frac{\partial \bar{u}}{\partial \bar{t}} + \bar{u}\frac{\partial \bar{u}}{\partial \bar{r}} + \bar{w}\frac{\partial \bar{u}}{\partial \bar{z}}\right) = -\frac{\partial \bar{p}}{\partial \bar{r}} + (\mu_{nf} + k)\left(\frac{\partial^2 \bar{u}}{\partial \bar{r}^2} + \frac{1}{\bar{r}}\frac{\partial \bar{u}}{\partial \bar{r}} - \frac{\bar{u}}{\bar{r}^2}\right) - k\left(\frac{\partial \bar{N}}{\partial \bar{z}}\right) \tag{16}$$

$$\rho_{nf}\left(\frac{\partial \bar{w}}{\partial \bar{t}} + \bar{u}\frac{\partial \bar{w}}{\partial \bar{r}} + \bar{w}\frac{\partial \bar{w}}{\partial \bar{z}}\right) = -\frac{\partial \bar{p}}{\partial \bar{z}} + (\mu_{nf} + k)\left(\frac{\partial^2 \bar{w}}{\partial \bar{r}^2} + \frac{1}{\bar{r}}\frac{\partial \bar{w}}{\partial \bar{r}} + \frac{\partial^2 \bar{w}}{\partial \bar{z}^2}\right) + \frac{k}{\bar{r}}\left(\frac{\partial\left(\bar{r}\bar{N}\right)}{\partial \bar{r}}\right) \tag{17}$$

$$\rho_{nf} J\left(\frac{\partial \bar{N}}{\partial \bar{t}} + \bar{u}\frac{\partial \bar{N}}{\partial \bar{r}} + \bar{w}\frac{\partial \bar{N}}{\partial \bar{z}}\right) = -2k\bar{N} - k\left(\frac{\partial \bar{w}}{\partial \bar{r}} - \frac{\partial \bar{u}}{\partial \bar{z}}\right) + \gamma\left(\frac{\partial}{\partial \bar{r}}\left(\frac{1}{\bar{r}}\frac{\partial\left(\bar{r}\bar{N}\right)}{\partial \bar{r}}\right) + \frac{\partial^2 \bar{N}}{\partial \bar{z}^2}\right) \tag{18}$$

$$(\rho c_p)_{nf}\left(\frac{\partial \bar{T}}{\partial \bar{t}} + \bar{u}\frac{\partial \bar{T}}{\partial \bar{r}} + \bar{w}\frac{\partial \bar{T}}{\partial \bar{z}}\right) = K_{nf}\left(\frac{\partial^2 \bar{T}}{\partial \bar{r}^2} + \frac{1}{\bar{r}}\frac{\partial \bar{T}}{\partial \bar{r}} + \frac{\partial^2 \bar{T}}{\partial \bar{z}^2}\right) \tag{19}$$

The pulsatile nature of the fluid flow is simulated using the following form of axial pressure gradient, following Fung [71]:

$$-\frac{\partial \bar{p}}{\partial \bar{z}} = A_0 + A_1 \cos(\omega_p \bar{t}) \tag{20}$$

where A_0 is the mean pressure gradient and A_1 is the amplitude of the pulsatile component which is responsible for systolic and diastolic pressures. The following boundary conditions are prescribed:

$$\begin{aligned}
&\bar{w}(\bar{r},\bar{t}) = 0,\ \bar{N}(\bar{r},\bar{t}) = 0,\ \bar{T}(\bar{r},\bar{t}) = 0 && at\ \bar{t} = 0\\
&\frac{\partial \bar{w}}{\partial \bar{r}} = 0,\ \frac{\partial \bar{N}}{\partial \bar{r}} = 0,\ \frac{\partial \bar{T}}{\partial \bar{r}} = 0 && at\ \bar{r} = 0\\
&\bar{w}(\bar{r},\bar{t}) = 0,\ \bar{N}(\bar{r},\bar{t}) = 0,\ \bar{T}(\bar{r},\bar{t}) = T_0 && at\ \bar{R}(\bar{z}) = 0
\end{aligned} \tag{21}$$

Introducing the following non-dimensional variables:

$$\begin{aligned}
&z = \frac{\bar{z}}{J_1},\ r = \frac{\bar{r}}{d_0},\ w = \frac{\bar{w}}{U_0}, u = \frac{\bar{u}J_1}{U_0\delta},\ h = \frac{\bar{h}}{d_0},\\
&p = \frac{{d_0}^2\bar{p}}{U_0 J_1 \mu_f},\ \alpha = \frac{\rho_f \omega_p {d_0}^2}{\mu_f},\ N = \frac{d_0\bar{N}}{U_0},\ J = \frac{\bar{J}}{{d_0}^2},\\
&\theta = \frac{(\bar{T} - T_0)}{T_0},\ \mathrm{Pr} = \frac{\mu_f c_p}{K_f}
\end{aligned} \tag{22}$$

Eqn. (22) is inserted into Eqns. (15) to (19), respectively, and the additional conditions adopted are:

$$(i)\ \mathrm{Re}\frac{\delta n^{\frac{1}{n-1}}}{J_1} << 1 \tag{23a}$$

$$(ii)\ \frac{d_0 n^{\frac{1}{n-1}}}{J_1} \sim O(1) \tag{23b}$$

Proceeding with the analysis, the appropriate equations describing the unsteady flow of micropolar blood in the case of the mild stenosis ($\frac{\delta}{d_0} << 1$) then emerge as:

$$\alpha\frac{\partial w}{\partial t} = -\frac{1}{\phi_1}\frac{\partial p}{\partial z} + \frac{1}{\phi_1}\left(\frac{1}{(1-\phi)^{2.5}} + k\right)\left(\frac{\partial^2 w}{\partial r^2} + \frac{1}{r}\frac{\partial w}{\partial r}\right) + \frac{k}{\phi_1}\frac{1}{r}\left(\frac{\partial (rN)}{\partial r}\right) \tag{24}$$

$$\alpha\frac{\partial N}{\partial t} = -\frac{k}{J\phi_1}\left(2N + \frac{\partial w}{\partial r}\right) + \frac{1}{\phi_1}\left(\frac{1}{(1-\phi)^{2.5}} + \frac{k}{2}\right)\frac{\partial}{\partial r}\frac{1}{r}\left(\frac{\partial (rN)}{\partial r}\right) \tag{25}$$

$$\alpha\frac{\partial \theta}{\partial t} = -\frac{K_{nf}}{K_f}\frac{1}{\phi_2}\frac{1}{\mathrm{Pr}}\left(\frac{\partial^2 \theta}{\partial r^2} + \frac{1}{r}\frac{\partial \theta}{\partial r}\right) \tag{26}$$

Here the dimensionless pressure gradient will be of the form $-\frac{\partial p}{\partial z} = B(1 + e\cos(2\pi ct))$, $\phi_2 = 1-\phi+\phi\frac{(\rho c)_s}{(\rho c)_f}$ and $\phi_1 = 1-\phi+\phi\frac{(\rho)_s}{(\rho)_f}$.

The dimensionless boundary conditions assume the form:

$$\begin{aligned} &w(r,t) = 0,\ N(r,t) = 0,\ \theta(r,t) = 0 && at\ t = 0 \\ &\frac{\partial w}{\partial r} = 0,\ \frac{\partial N}{\partial r} = 0,\ \frac{\partial \theta}{\partial r} = 0 && at\ r = 0 \\ &w(r,t) = 0,\ N(r,t) = 0,\ \theta(r,t) = 1 && at\ R(z) = 0 \end{aligned} \tag{27}$$

The non-dimensional form of the stenosis geometry is now described as:

$$R(z) = (1 + z\tan\psi)\left[1 - \eta'\left((z - J_3) - (z - J_3)^n\right)\right] \qquad J_3 \le z \le J_3 + 1 \tag{28}$$

With $\eta' = \delta^* \frac{n^{\frac{n}{n-1}}}{n-1}$, $\delta^* = \delta d_0$ *and* $J_3 = \frac{J_0}{J_1}$

In order to calculate the volumetric flow rate (Q), wall shear stress (WSS) and the resistance to flow (λ - hemodynamic impedance), the appropriate expressions in non-dimensional form are:

$$Q = R^2 \int_0^1 w\, x\, dx \tag{29a}$$

$$WSS = \frac{1}{\alpha^2 R}\left(\mu_{nf} + K\right)\frac{\partial w}{\partial x} + \frac{K}{\alpha^2} N \tag{29b}$$

$$\lambda = \frac{B(1 + e\cos(2\pi ct))}{R^2 \int_0^1 w\, x\, dx} \tag{29c}$$

3. NUMERICAL COMPUTATIONS WITH FREEFEM++ CODE

The non-dimensional boundary value problem is derived i.e., Eqns. (24)-(26) with boundary conditions (27) is still quite formidable owing to strong nonlinearity, the coupling of different variables, and two space variables. A robust computational scheme is, therefore, essential to obtain fast and rapidly convergent solutions. Here the finite element method (FEM) with the variational approach, as available in the FreeFEM++ software [69], has been used. The weak formulation of the partial differential equation system (24)-(26) is derived by defining the function spaces:

$$\begin{aligned} X &= \left\{ u \in \left(H_1(\Omega)\right) \middle| u = a \text{ on } \Gamma_{in}, u = 0 \text{ on } \Gamma_{wall} \right\} \\ Q^{'} &= \left\{ u \in \left(H_1(\Omega)\right) \middle| u = 0 \text{ on } \Gamma_{in} \cup \Gamma_{wall} \right\} \end{aligned} \tag{30}$$

The weak form of Eqns. (24) - (26) is obtained by determining w, N ∈ X, and Θ ∈ P such that every $u_1, u_2 \in Q$ and $p_1 \in P$ where $P = L^2(\Omega)$. A fundamental aspect of the current modeling is to obtain the *weak form* of the above system of Eqns. (24)-(26). To achieve smoothness of a solution which is bounded due to the weaker restriction, these differential equations cannot be solved directly. Therefore, the finite-dimensional subspaces have to be defined as $Q_h \subset Q$ and $P_h \subset P$. Consider the finite dimensional approximations as $u_{1h}, u_{2h} \subset Q_h$ and $p_{1h} \subset P_h$. In view of the finite dimensional approximations, the set of Eqns. (24)-(26) becomes:

$$\int_{\Omega}\alpha\frac{\partial w}{\partial t}\cdot u_{1h}dr=-\int_{\Omega}\frac{1}{\phi_1}B(1+e\cos(2\pi ct)\cdot u_{1h}dr$$
$$+\int_{\Omega}\frac{1}{\phi_1}\left(\frac{1}{(1-\phi)^{2.5}}+k\right)\left(\frac{\partial^2 w}{\partial r^2}+\frac{1}{r}\frac{\partial w}{\partial r}\right)\cdot u_{1h}dr+\int_{\Omega}\frac{k}{\phi_1}\frac{1}{r}\left(\frac{\partial(rN)}{\partial r}\right)\cdot u_{1h}dr \quad (31)$$

$$\int_{\Omega}\alpha\frac{\partial N}{\partial t}\cdot u_{2h}dr=-\int_{\Omega}\frac{k}{J\phi_1}\left(2N+\frac{\partial w}{\partial r}\right)\cdot u_{2h}dr$$
$$+\int_{\Omega}\frac{1}{\phi_1}\left(\frac{1}{(1-\phi)^{2.5}}+\frac{k}{2}\right)\frac{\partial}{\partial r}\frac{1}{r}\left(\frac{\partial(rN)}{\partial r}\right)\cdot u_{2h}dr \quad (32)$$

$$\int_{\Omega}\alpha\frac{\partial\theta}{\partial t}\cdot p_{1h}dr=-\int_{\Omega}\frac{K_{nf}}{K_f}\frac{1}{\phi_2}\frac{1}{\Pr}\left(\frac{\partial^2\theta}{\partial r^2}+\frac{1}{r}\frac{\partial\theta}{\partial r}\right)\cdot p_{1h}dr \quad (33)$$

Eqns. (31)-(33) with boundary conditions (28) are solved numerically using the variational finite element method in FreeFEM++. We have adopted an *unstructured fixed mesh* optimized after extensive mesh independence tests. The final mesh comprises **27,746** piecewise linear triangular elements (P2) and **56,033** nodes for the *divergent artery section*, **17,876** piecewise linear triangular elements (P2) and **36,291** nodes for the *convergent artery section* and **23,214** piecewise linear triangular elements (P2) and **46,969** nodes for the *non-tapered artery section* as shown in **Figures** 2(a), 2(b) and 2(c) respectively. The mesh is designed by taking advantage of the automatic FreeFEM++ mesh generator based on the Delaunay-Voronoi algorithm. Further details are given in Bathe [73]. The non-linear system of governing equations has been solved by employing the **G**eneralized **M**inimal **Res**idual (GMRES) iteration method. In the fixed mesh, a minimum step size $h_{\min}$ of 0.014192 is considered with the tolerance of computation $<10^{-6}$ for all simulations. In **Figures 2(a), 2(b) and 2(c),** the *level (degree) of stenosis* is 40% in the diverging tapering artery, 60% in converging tapering artery and a little more than 50% in the non-tapered artery respectively.

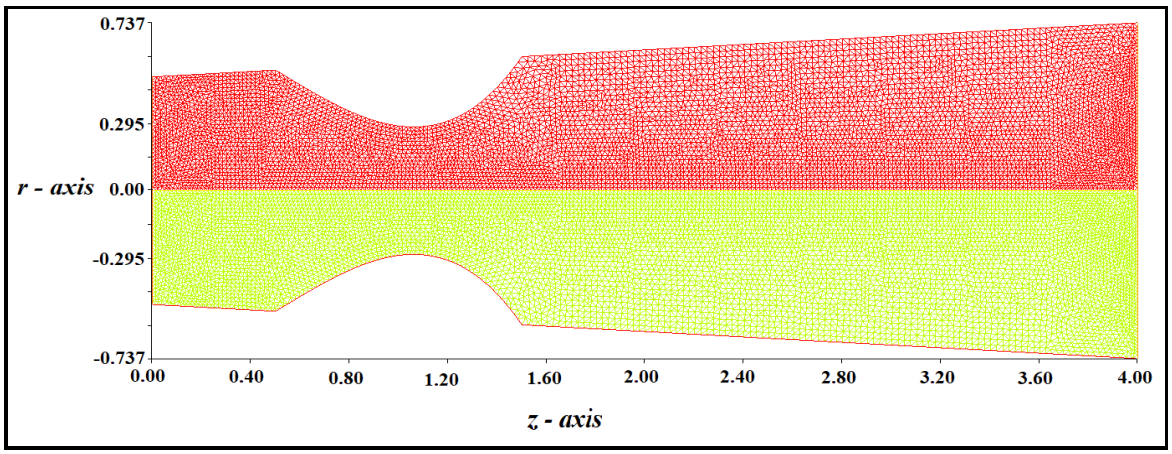

Figure 2(a). Unstructured fixed mesh of triangular elements ($\psi = 0.0592880$)

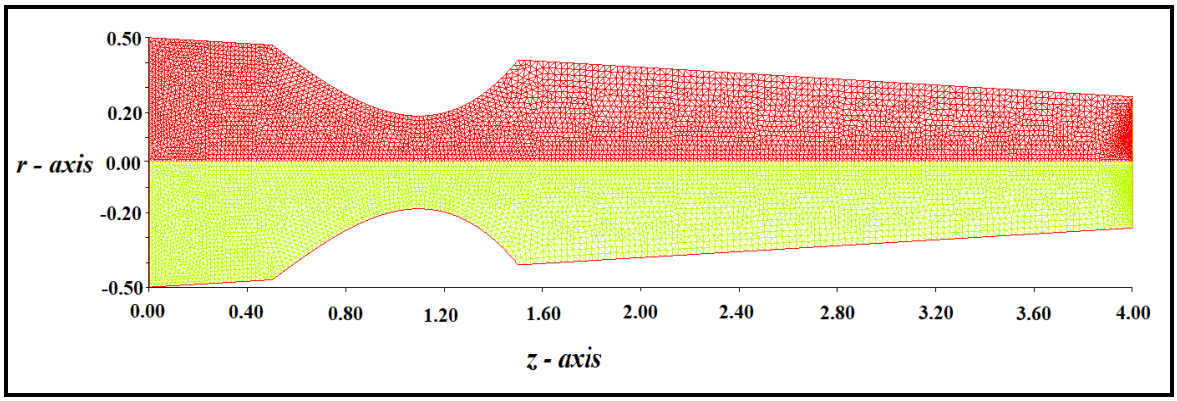

Figure 2(b). Unstructured fixed mesh of triangular elements ($\psi = -0.0592880$)

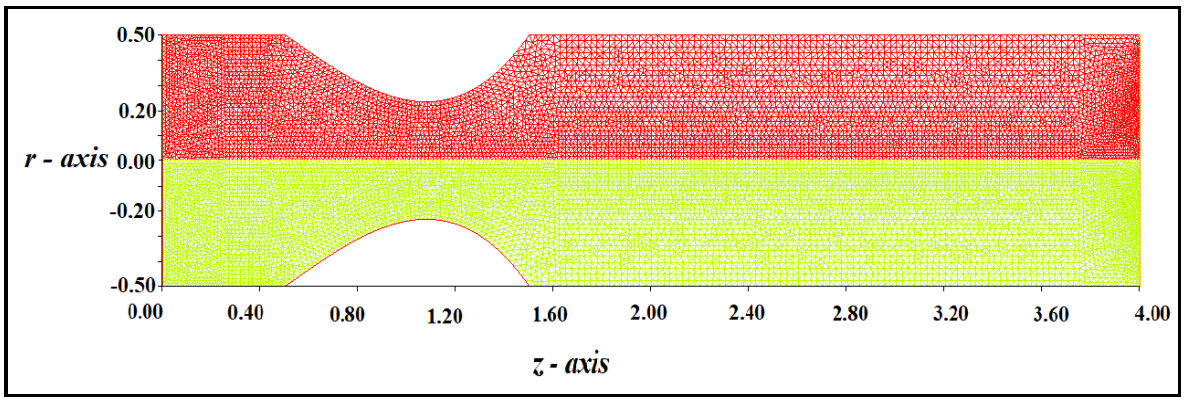

Figure 2(c). Unstructured fixed mesh of triangular elements ($\psi = 0.00$)

4. MESH INDEPENDENCE ANALYSIS

By conducting several different finite element mesh (grid) distribution tests, it may be established whether the calculated numerical results are grid-independent or not. The numerical values for wall shear stress at stenosis in all three tapering geometries, for various designs comprising unstructured fixed mesh elements with vertices and triangular elements, are provided in **Figure 3**. Seven different mesh distributions have been tested to ensure the simulated numerical results are *mesh independent*. Eventually, the selected mesh for the present calculations consisted of **27,746** triangular elements and **56,033** nodes for the *divergent artery section*, **17,876** triangular elements and **36,291** nodes for the *convergent artery section and* **23,214** triangular elements and **46,969** nodes for the *convergent artery section* respectively (simulation number 6 in **Table 2**). From Table 2 and figure 3, it is evident that increasing the mesh element density beyond this design does not modify the numerical values for non-dimensional wall shear stress significantly in the domain with the parametric values prescribed i.e. $\phi = 0.3, \alpha = 2.0, B = 1.0, e = 1.0, k = 0.3, Pr = 14$ *and* $t = 0.2$ *at* $r = 0.190$, for $\psi = -0.0593$, $\psi = 0.0593$ *and* $\psi = 0.00$, respectively.

Table 2 (a). Grid Independency analysis with $\psi = 0.0593$, $\phi = 0.3$, $\alpha = 2.0, \mathrm{B} = 1.0$, $\mathrm{e} = 1.0$, $\mathrm{k} = 0.3$, $\mathrm{Pr} = 14$ *and* $t = 0.2$ *at* $r = 0.190$, $z = 1.10$

Simulation No.	Number of Elements	Number of Nodes	Wall shear stress (Stenosis)
1.	8026	16363	3.6301
2.	8894	18109	3.0439
3.	13020	26441	1.355
4.	22448	47417	1.1458
5.	23448	47547	0.70632
6.	**27746**	**56033**	**0.87855**
7.	35514	71629	0.88798

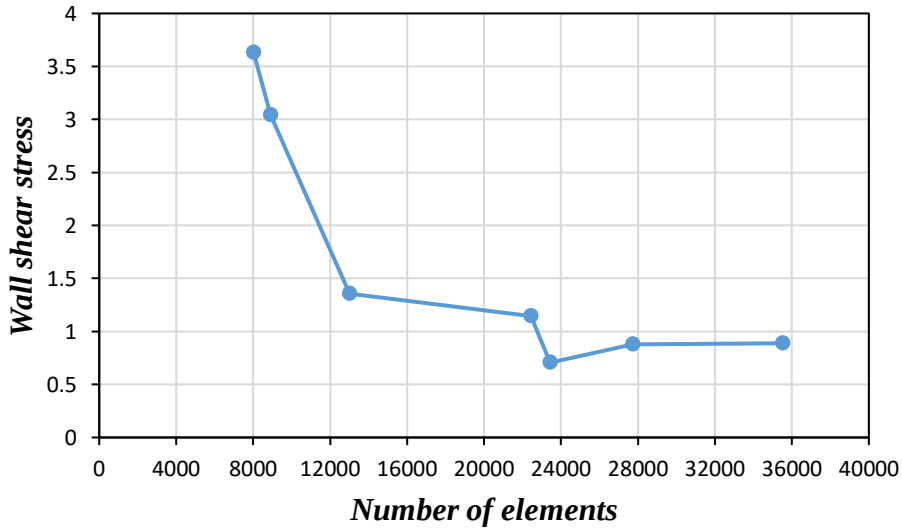

Figure 3(a): Grid Independence study (wall shear stress)

Table 2 (b). Grid Independency analysis with $\psi = -0.0593$, $\phi = 0.3$, $\alpha = 2.0, \mathrm{B} = 1.0$, $\mathrm{e} = 1.0$, $\mathrm{k} = 0.3$, $\mathrm{Pr} = 14$ *and* $t = 0.2$ *at* $r = 0.190$, $z = 1.10$

Simulation No.	Number of Elements	Number of Nodes	Wall shear stress (Stenosis)
1.	5222	10755	-2.8284
2.	5393	10952	-1.2126
3.	5952	12225	3.1671
4.	14296	29113	3.6699
5.	15084	30649	1.2426
6.	17876	**36291**	**1.3458**
7.	23330	47201	1.296

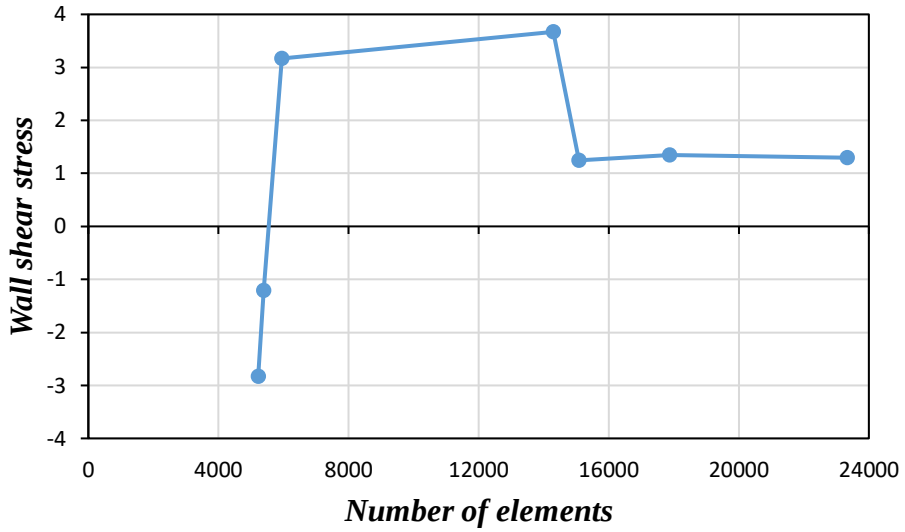

Figure 3(b): Grid Independence study (wall shear stress)

Table 2 (c). Grid Independency analysis with $\psi = 0.00$, $\phi = 0.3$, $\alpha = 2.0$, B = 1.0, e = 1.0, k = 0.3, Pr = 14 *and* $t = 0.2$ *at* $r = 0.190$, $z = 1.10$

Simulation No.	Number of Elements	Number of Nodes	Wall shear stress (Stenosis)
1.	6494	13279	-0.69352
2.	7748	15917	-2.3116
3.	10586	21473	-3.5629
4.	18176	36873	-2.868
5.	19222	38925	1.5278
6.	23214	**46969**	**3.0533**
7.	29816	60233	3.1003

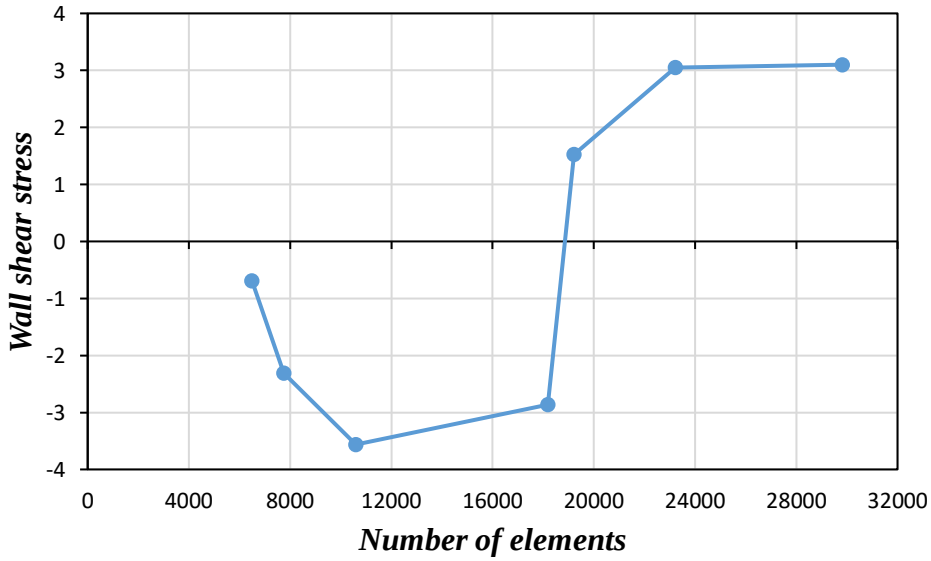

Figure 3(c): Grid Independence study (wall shear stress)

5. RESULTS AND DISCUSSION

In this section, the quantitative effect of selected parameters i.e., Eringen micropolar vortex viscosity material parameter (K), Prandtl number (Pr), concentration (ϕ), tapering angle (ψ), and pulsatile constants ($\boldsymbol{B}$ and $\boldsymbol{e}$), on the velocity, temperature and micropolar rotational velocity (Eringen micro-rotation) with the variation of time are examined in detail. The results are all visualized via tables, contour plots, and graphs. In the computations, the default values of various parameters are as documented in **Table 3**.

Table 3: Prescribed parameter values implemented in FREEFEM++ computations

Parameter	n	ψ	δ	Pr	L	α	B	e	K_f	ρ_f	c_f
Values	3	0.0592880	0.310	25	4.0	2.0	4.0	1.0	0.492	19320	3594

Table 4: Comparison of dimensionless velocity (w) values, using the present scheme with published results for $z = 0.7, \delta = 0.1, k = 0.1, \alpha = 2.0, B = 2.0, e = 1.0, K = 0.1$.

r - axis	**Velocity values (w) for a converging tapering artery ($\psi = -0.1$) with symmetric (composite) stenosis**		**Correlation coefficient (cc) and p-value**
	FDM solutions of Ali *et al.* [16]	**Present results using FREEFEM++ (variational approach)**	
0.1889	0.0845	0.0841	cc = 0.996920 and p-value = 7.2836E-08
0.2779	0.1245	0.12133	
0.36668	0.1421	0.14615	
0.4557	0.1437	0.14615	
0.5447	0.1335	0.13374	
0.6336	0.1128	0.10892	
0.7225	0.0827	0.0841	
0.8115	0.0448	0.046874	

To validate the FREEFEM++ code which has been adopted to simulate the problem, benchmarking against the published finite difference results obtained by Ali *et al.* [16] for velocity in viscous blood flow is conducted with the comparisons displayed in **Table 4**. Evidently a significant strong correlation is achieved testifying to the accuracy of the FREEFEM++ code. Confidence in the finite element simulations is therefore justifiably very high.

5.1 Effect of different metallic nanoparticles:

Figures 4(a) – 4(b) depict the effect of different metallic nanoparticles, i.e., Gold (Au), Copper (Cu), Alumina (Al_2O_3), Titanium oxide (TiO_2) on the temperature distribution for the *converging tapered arterial section* along the radial direction at the throat of stenosis for a fixed time. The temperature initially decreases with radial distance from the midline and subsequently is elevated in magnitude towards the arterial wall. For gold nanoparticles, the temperature is evenly distributed compared to the other metallic nanoparticles i.e.; a more homogenous distribution is achieved. However, an increment in time shows a monotonic decrement in the temperature distribution, indicating that the blood flow regime is cooled with progress in time.

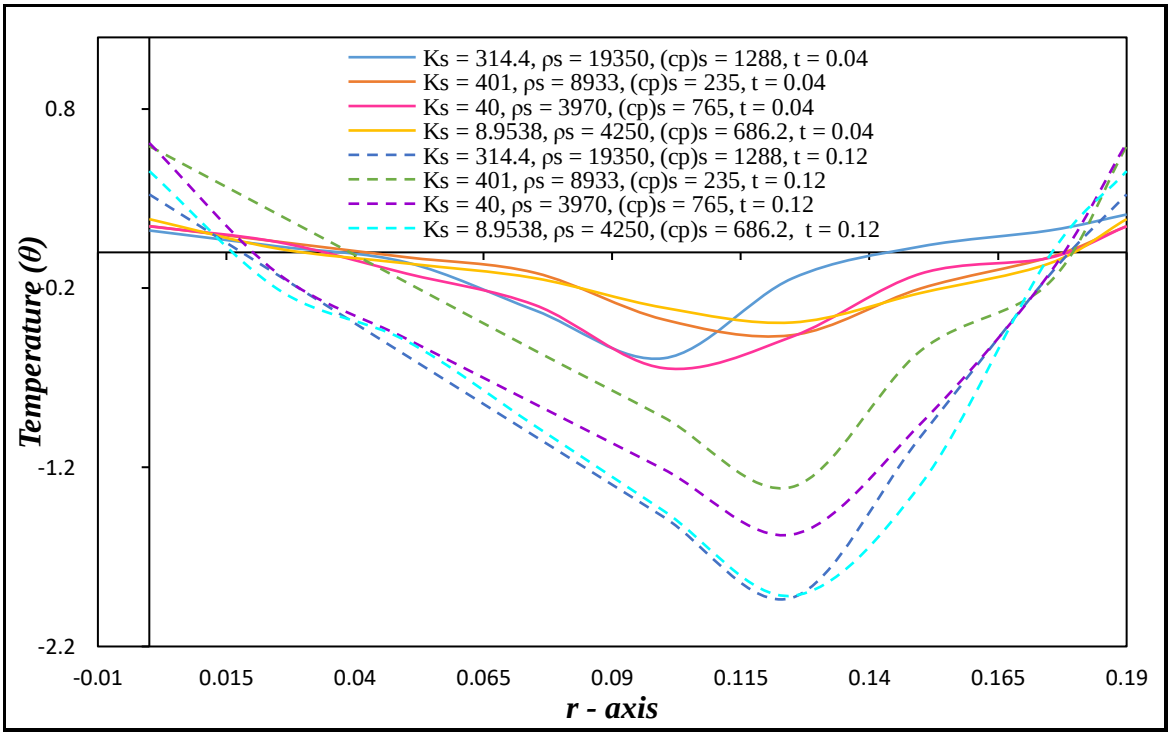

Figure 4(a): Effect of metallic nanoparticle on temperature distribution when $\psi = -0.06, z = 1.10, \alpha = 2.0,$ $e = 1.0, Pr = 25.$

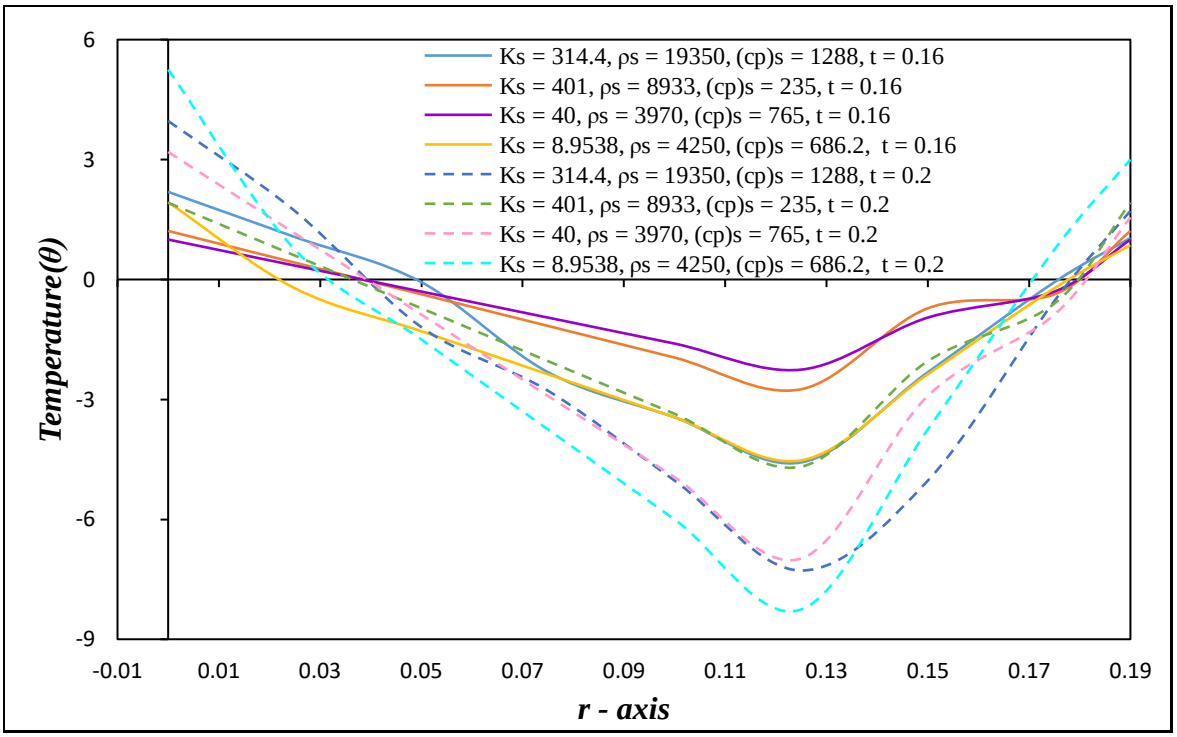

Figure 4(b): Effect of metallic nanoparticle on temperature with $\psi = -0.06, z = 1.10, \alpha = 2.0, e = 1.0, Pr = 25.$

Figures 5 and 6 illustrate the impact of different metallic nanoparticles on flow characteristics. Figure 5 displays the linear velocity profile with time whereas figure 6 shows a comparison of micro-rotational velocity (N) at different times for Gold (Au) and other nanoparticles, respectively. All metallic nanoparticles in figure 5 consistently produce a periodic motion (pulsatile profiles); however, only gold and copper exhibit a marked increment as we move forward in time, whereas Alumina and titanium oxide generate exactly the opposite behaviour. The micro-rotational velocity in figure 6, again captures the pulsatile nature of the flow with time progression. Significantly higher amplitudes of micro-rotation are associated with the non-tapered section compared with the diverging section; however, the latter also produces higher magnitudes than the converging case, which corresponds to minimal micro-rotation amplitudes. The negative values of micro-rotation imply a reversal in the spin of the micro-elements i.e., angular velocity in the opposite direction to positive values. Therefore, the geometric nature of the arterial zone exerts a profound influence on microstructural flow characteristics which cannot be captured, as elaborated earlier, with simpler rheological models. It is also noteworthy that at high time values, the micro-rotation magnitudes in the diverging section approach comparable values to the non-tapered artery; however, the values in the former are much lower at all other times. The *unsteady* model is, therefore, also a very important feature in appraising more accurately the microstructural rheology features of real blood.

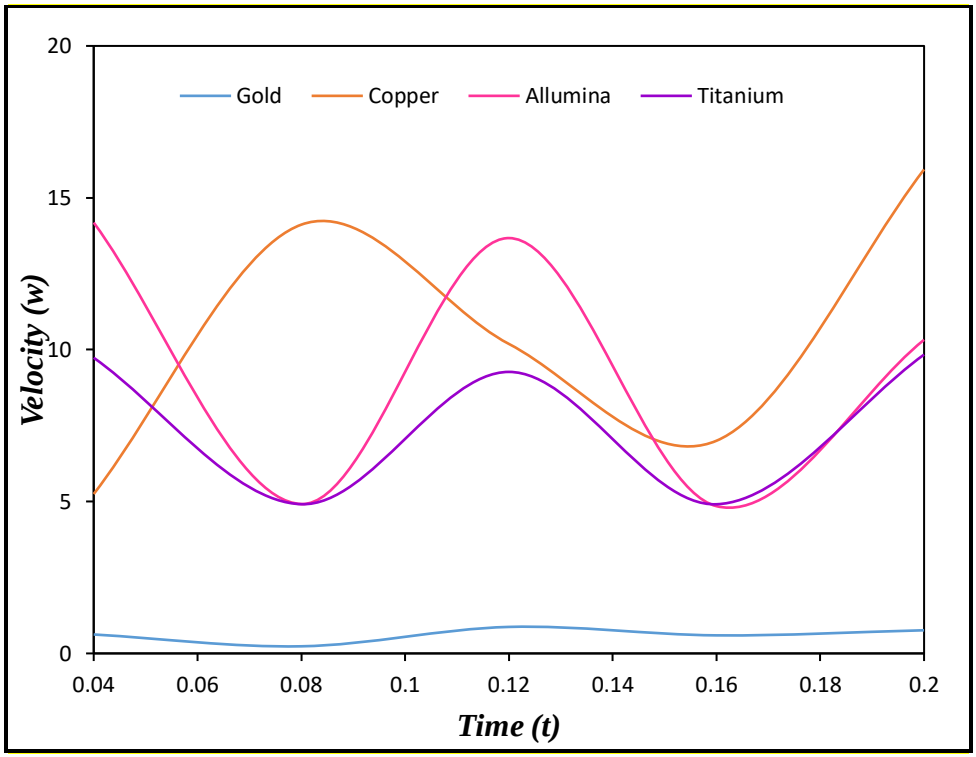

Figure 5: Effect of metallic nanoparticle on velocity profile for $\psi = -0.06,\ \alpha = 2.0, B = 4.0,\ e = 1.0,$ $\phi = 0.1, z = 1.10$ *and* $r = 0.250$

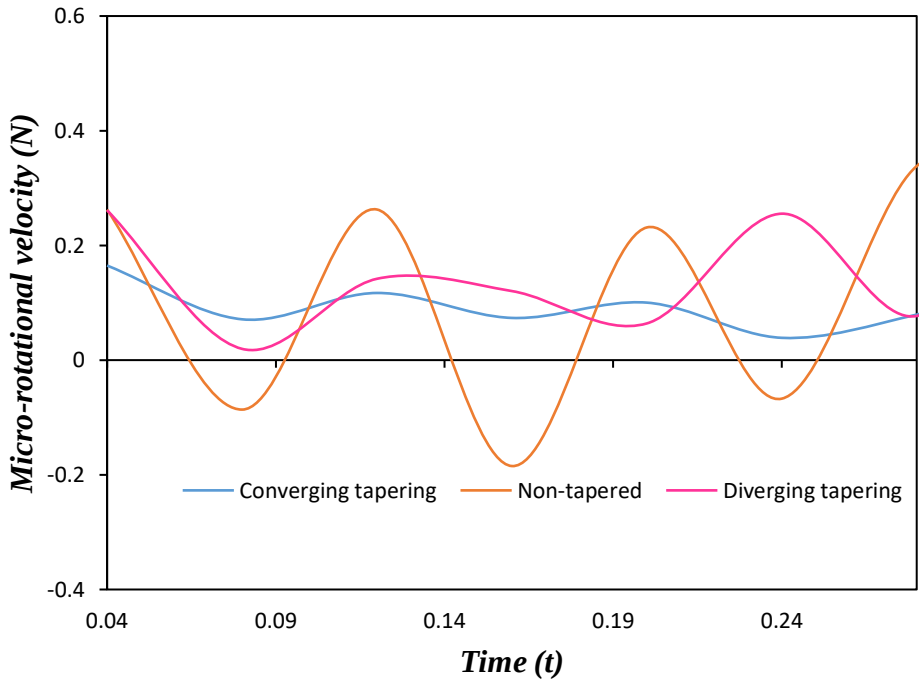

Figure 6: Effect of ***tapering angle*** on micro-rotational velocity for *Gold (Au),* $z = 1.10, \delta = 0.310, \Pr = 25,$ $\alpha = 2.0, r = 0.150, B = 4.0, e = 1.0$

5.2 Effect of Prandtl number

Figure 7 illustrates the effect of the Prandtl number on the micro-rotational velocity (N) with a temporal variation on a fixed point in the arterial segment, which is at the throat of the stenosis. It can be observed that a greater Prandtl number induces a reduction in the micro rotational velocity decreases; the maximum value of micro-rotational velocity again corresponds to the case of a non-tapered artery. Prandtl number is the key parameter dictating heat transfer in the blood. It is inversely proportional to thermal conductivity. *Pr = 14*, therefore, implies that thermal conductivity is half for the case of *Pr = 7*. The momentum to energy diffusion rate ratio for *Pr = 14* is twice that for *Pr =7*. Although only forced convection is considered and there are no coupling terms between the linear velocity and temperature fields in Eqns. (24) and (26), there is a strong coupling between the linear momentum Eqn. (24) and the micro-rotation field (N) via the term $-\frac{k}{J\phi_1}\left(2N+\frac{\partial w}{\partial r}\right)$. The enhancement in linear momentum diffusion with a higher Prandtl number generates a damping effect on microelement spin. However, with progression in time, there is a significant boost in micro-rotation, indicating that microelement gyration is encouraged with time in the arterial regime. **Fig. 8** also presents colored contours for three tapered angles at different periods. It is evident again that the maximum value of micro-rotational velocity is achieved for the *non-tapered arterial* case. The contour plots demonstrate that micro-rotational velocity contour magnitudes are suppressed with a greater time-period; furthermore, there is a decrement in micro-rotation magnitudes with distance from the core region to the wall in all cases. The darker red zones are progressively eliminated and replaced with green and then blue zones indicating a significant drop on micro-rotation magnitudes with time.

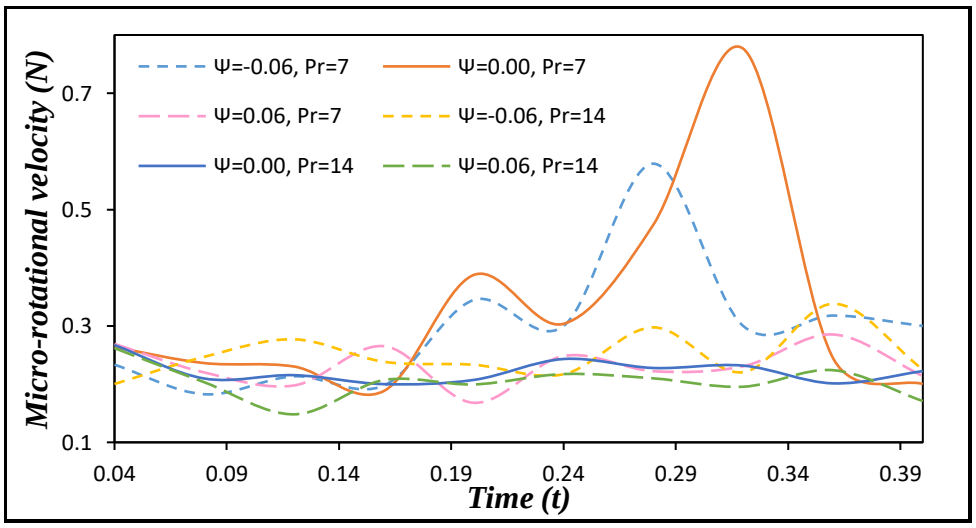

Figure 7: Effect of ***Pr*** on micro-rotational velocity for *Gold (Au),* $\phi = 0.5, k = 0.3, \alpha = 2.0, B = 2.0,$ $e = 1.0, r = 0.100, z = 1.00$

Additionally, it is pertinent to note that the strong circulation zones appearing both upstream and downstream of the stenosis at *short times* are progressively eliminated with more significant times, and a strong core zone is synthesized with elongated micro-rotation circulation zones far downstream of the diverging section of the arterial segment.

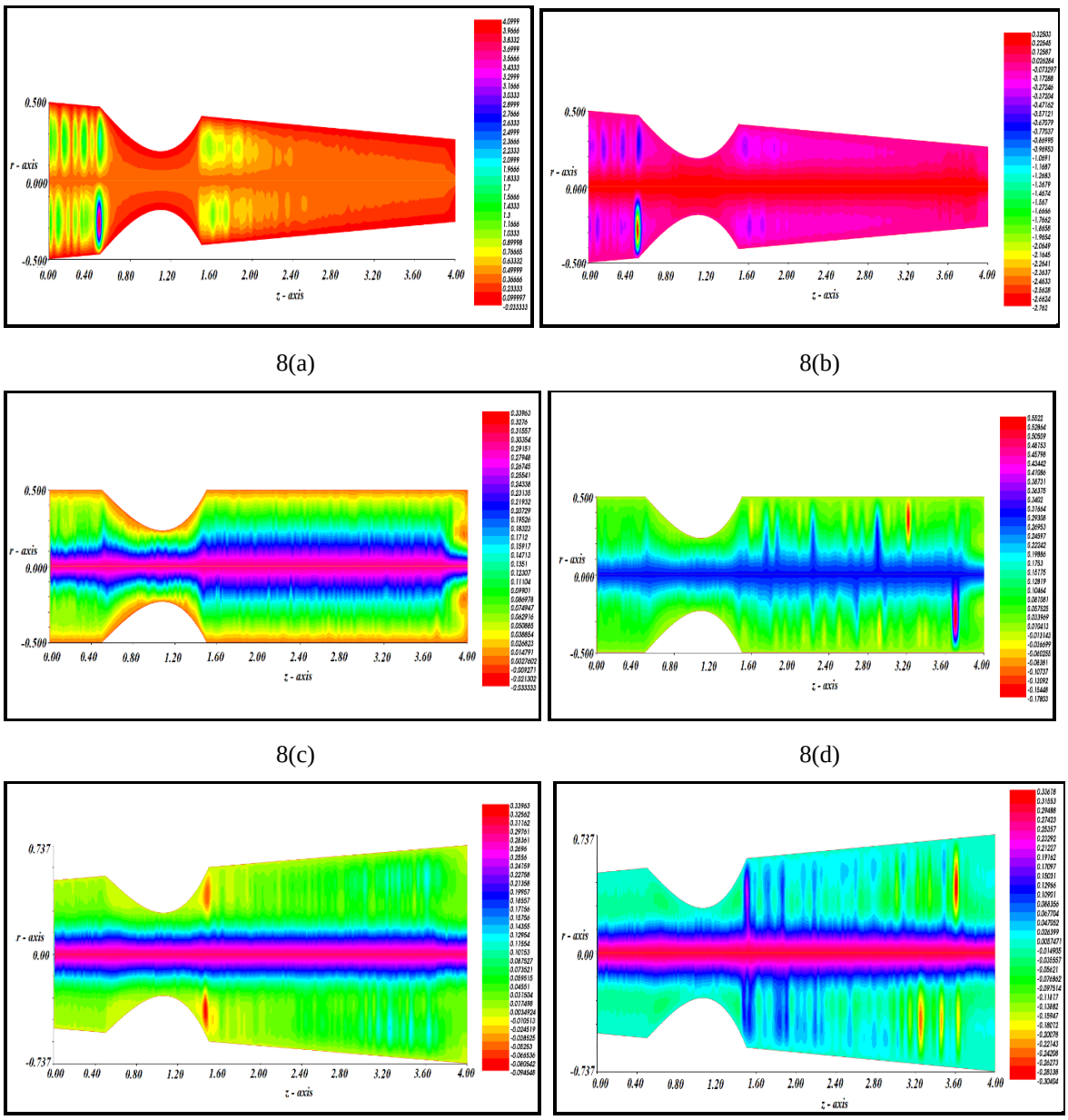

8(a) 8(b)

8(c) 8(d)

8(e) 8(f)

Figure 8: Micro-rotational velocity profile for *Gold (Au) when* $\phi = 0.3, \mathrm{Pr} = 14, \alpha = 2.0, B = 2.0, e = 1.0, k = 0.3$ at $(a)\psi = -0.06,\ t = 0.2,\ (b)\psi = -0.06,\ t = 0.4,\ (c)\psi = 0.00,\ t = 0.2,\ (d)\psi = 0.00,\ t = 0.4, (e)\psi = 0.06,\ t = 0.2,$ $(f)\psi = 0.06,\ t = 0.4$

5.3 Effect of α (Womersley number of non-Newtonian fluid), B (dimensionless pulsatile constant), k and e

Figure 9 shows the variation in pressure gradient ($\partial p/\partial z$) over time (t) for the two different values of pulsatile constants ***B*** and ***e***. The graph shows that the pressure gradient value is directly proportional to ***B*** and ***e***; hence an increment in both ***B*** and ***e*** increases the value of the pressure gradient. However, there is a strong decay in the axial pressure gradient with progression in time, indicating that momentum is depleted in the arterial regime as time passes. Therefore, the pulsatile effect weakens with time, which is characteristic of real blood flows [71].

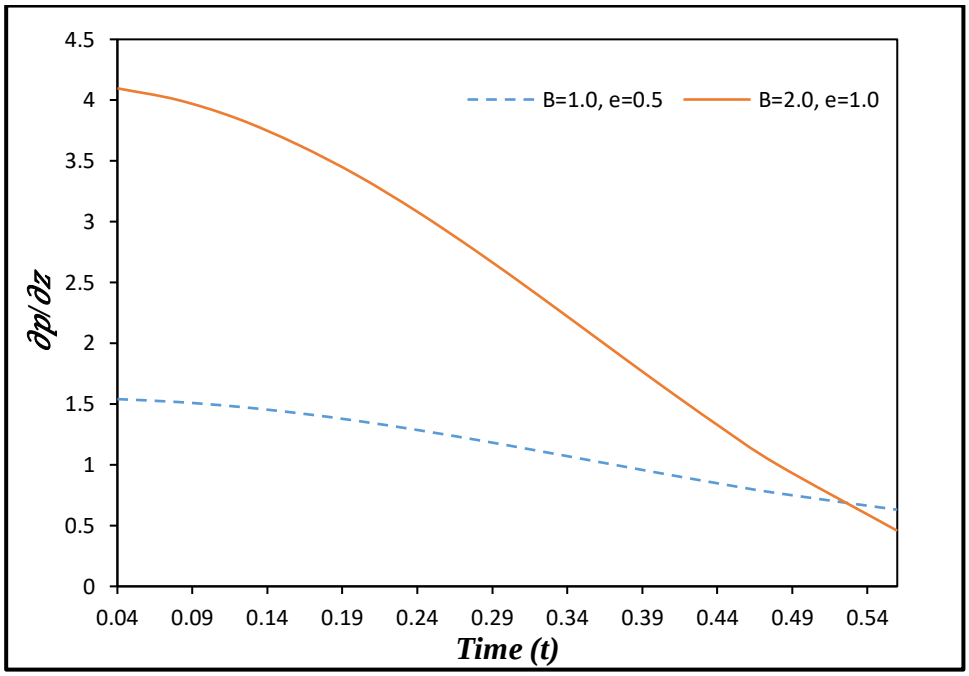

Figure 9: Effect of ***B and e*** on Pressure gradient for *Gold (Au),* $\phi = 0.5, k = 0.3, \alpha = 2.0, r = 0.100,$ $, z = 1.00, \Pr = 7.0$.

Figure 10 shows the evolution in micro-rotational velocity with an increment in Womersley number (α). Evidently, there is strong damping of microelement spin (micro-rotation) with increasing Womersley number, a trend which is sustained at all times. Womersley number is a dimensionless expression which is very popular in hemodynamics; it represents *the relative contribution of pulsatile flow frequency to viscous effects*. In large vessels e.g., the aorta, α can range between 15 and 20 [71]; however, it is much smaller (< 5) in microvascular and capillary vessels, as considered in the present simulations for which α *=2, 3*. The linear velocity field (w) typically exhibits a periodic topology near the arterial walls, which resembles the Stokes layer on an oscillating flat plate. Linear momentum is generally suppressed with the

Womersley parameter since viscous effects become more dominant. This simultaneously inhibits gyratory motions of the micro-elements in the blood and produces angular deceleration, as observed in Fig. 10. Although not shown, the linear velocity close to the walls features a layer of thickness O (α^{-1}), and the velocity adjusts rapidly to zero. Furthermore, the phase of the time oscillation varies quickly with position across the layer. The exponential decay of the higher frequencies is faster when $\alpha >> 1$, a relatively small steady component of the pressure gradient gives rise to a steady velocity which is relatively much larger. A similar insight has been provided by Mazumdar [72]. Clearly therefore viscous effects attain some significance with time, and this serves to damp the micro-rotation velocity. With lower α, the pulsatile nature is amplified in the micro-rotation field.

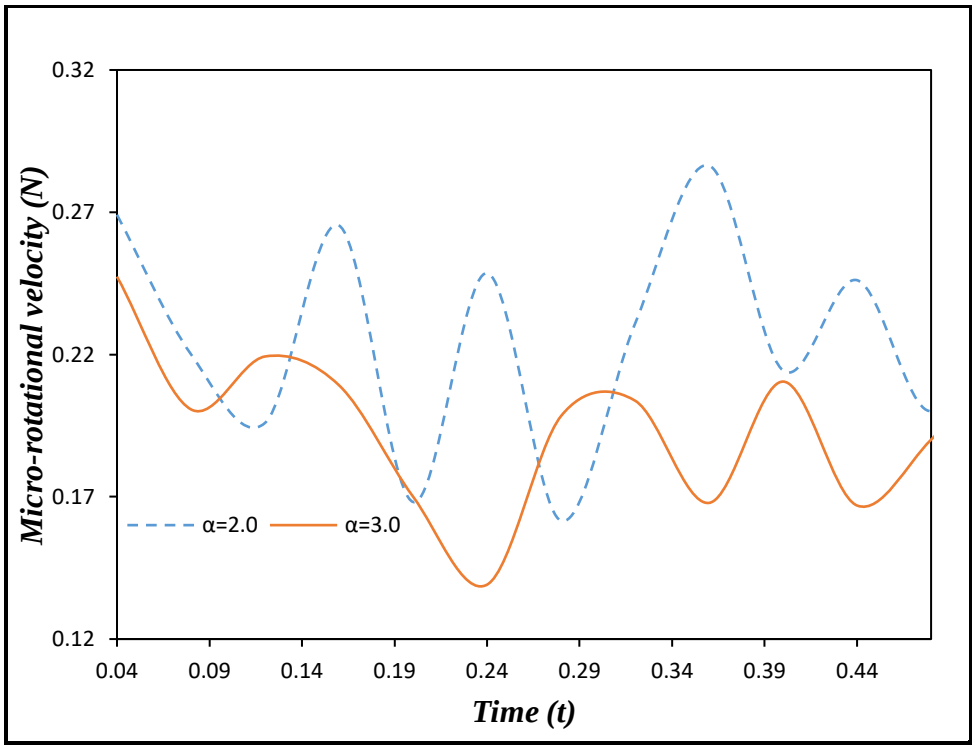

Figure 10: Effect of α on micro-rotational velocity for *Gold (Au)*, $\phi = 0.5, k = 0.3, B = 1.0, e = 0.5,$ $r = 0.100, z = 1.00, \Pr = 7.0$

Figure 11 depicts the variation in micro-rotational velocity (N) over a time period (t) for the three different values of the Eringen micropolar vortex viscosity parameter (k). This parameter defines the ratio of micropolar vortex viscosity to Newtonian dynamic viscosity. A significant enhancement in the value of micro-rotational velocity can be seen with a rise from $k = 0.1$ to $k = 0.5$ in converging tapered artery case, for large times, although the reverse behaviour is computed at shorter times. Therefore, the transient nature of the flow has a substantial influence on the impact of micropolar vortex viscosity on the gyratory motions of

microelements. There is no single consistent response computed, at all times, which further endorses the necessity for time-dependent mathematical models in hemodynamics [72]. Marked damping in the micro-rotation is observed at $k = 0.3$, implying again that there is a nonlinear relationship between the micropolar vortex viscosity and the microelement gyration i.e., the response to increment in micropolar vortex viscosity is not merely a linear one.

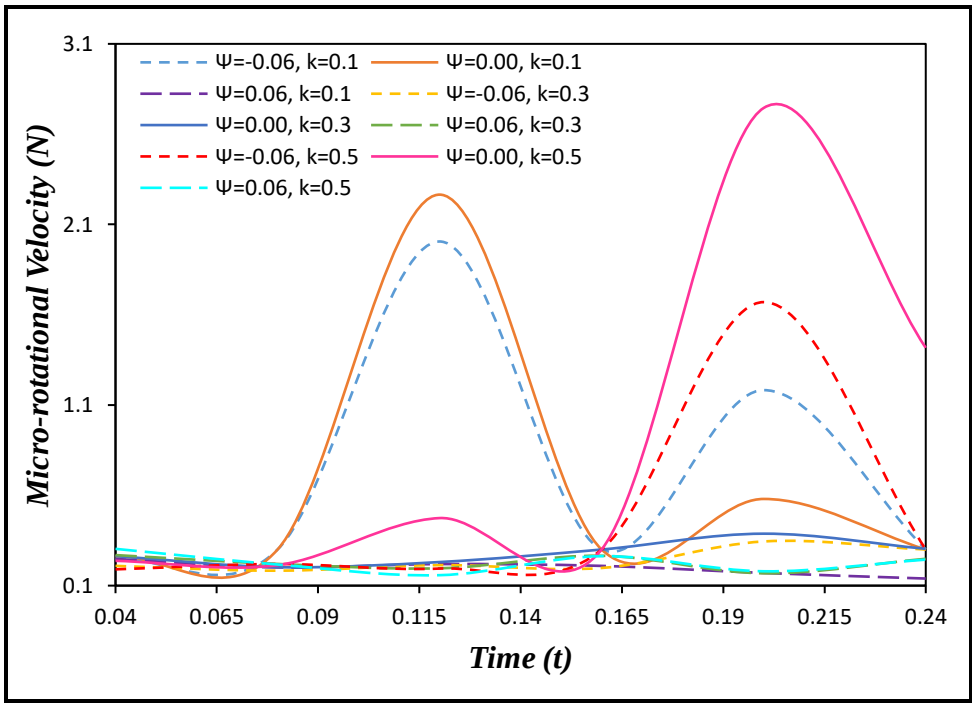

Figure 11: Effect of ***k*** on micro-rotational velocity for *Gold (Au),* $\phi = 0.5, \alpha = 2.0, B = 1.0, e = 0.5,$ $r = 0.100, z = 1.00, \Pr = 7.0$.

Figure 12 presents the variation in linear velocity profile (w) for the two different values of pulsatile constants **B** and **e**. The maximum value of velocity arises for the case of a converging tapering artery; as *the vessel becomes more extensive, the velocity decreases,* i.e., the diverging arterial section. In both these cases, the velocity is positive; however, strong flow reversal is induced for the non-tapered segment, manifesting in negative velocity. These patterns are maintained at all-time values and concur with many other hemodynamics investigations, including Devanathan and S. Parvathamma [47] and Samad [50].

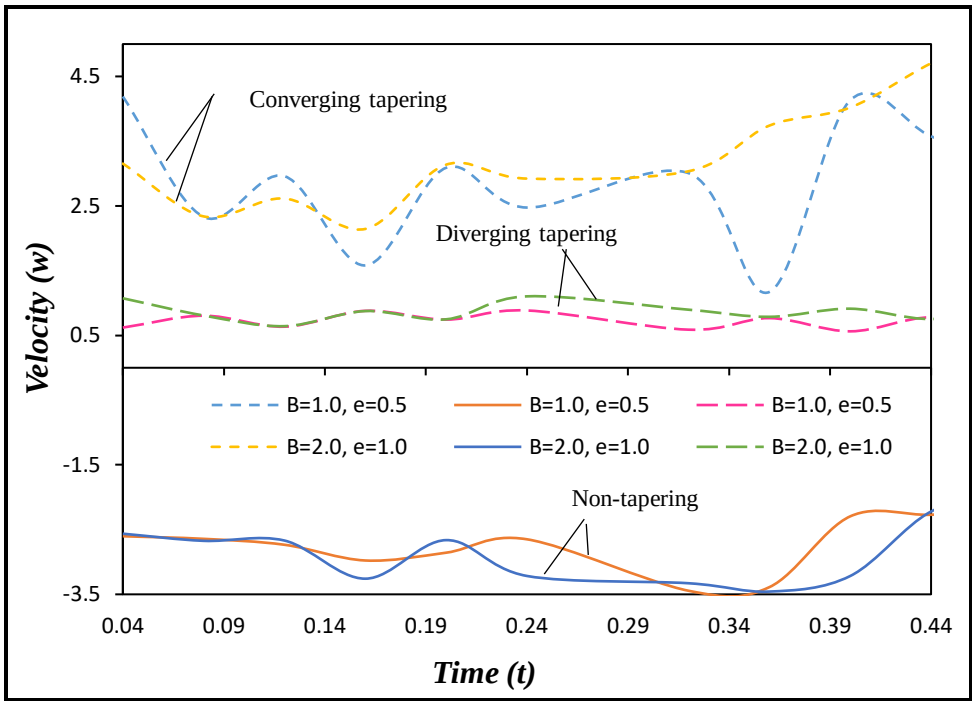

Figure 12: Effect of ***B and e*** on velocity for *Gold (Au)*, $\phi = 0.5, \alpha = 2.0, k = 0.3,\ r = 0.100,$ $z = 1.00, \Pr = 7.0$

Figures 13 to 17 are drawn for different values of the Womersley parameter (α) and pulsatile constants (***B*** and ***e***). Figures 13 - 14 correspond to micro-rotational velocity (*N*), and figures 15 – 17 to linear velocity (*w*) distribution over the whole arterial segment. Figures 13 and 14 show that by increasing the pulsatile constant, the pulsatile nature of fluid particle increases, and also, the value of micro-rotational velocity increases while moving forward in time for a diverging tapering artery in comparison with a converging tapering and non-tapered artery. This is attributable to the greater space afforded to microelements in the diverging section, which assists in their spinning. However, figures 16 and 17 exhibits the opposite nature as the *linear velocity* increases with the increment in pulsatile constants (***B*** and ***e***) but only for the converging and non-tapering one; linear flow deceleration is induced for the diverging artery since by virtue of continuity (mass conservation) larger cross-section reduces flow velocities. **Figure 15** visualizes the velocity evolution with time for different values of the Womersley parameter (α), and it is apparent that linear velocity decreases as the value of α increases.

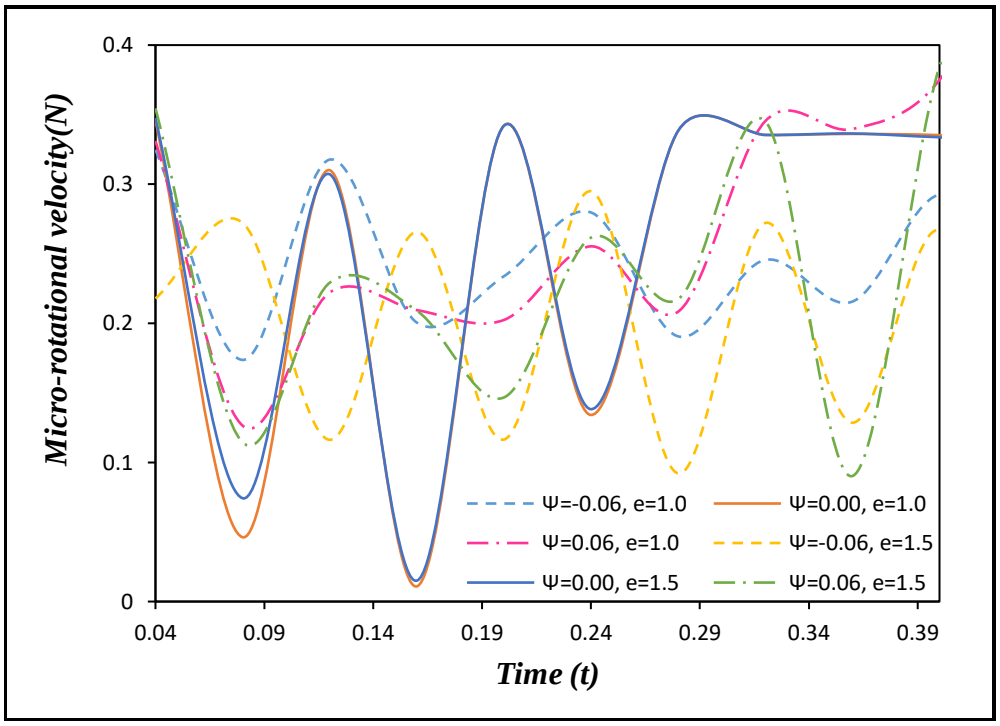

Figure 13: Effect of ***e*** on micro-rotational velocity profile for Gold (Au), $z = 1.10, \delta = 0.310, \Pr = 25,$ $r = 0.100, B = 4.0, \alpha = 2.0$

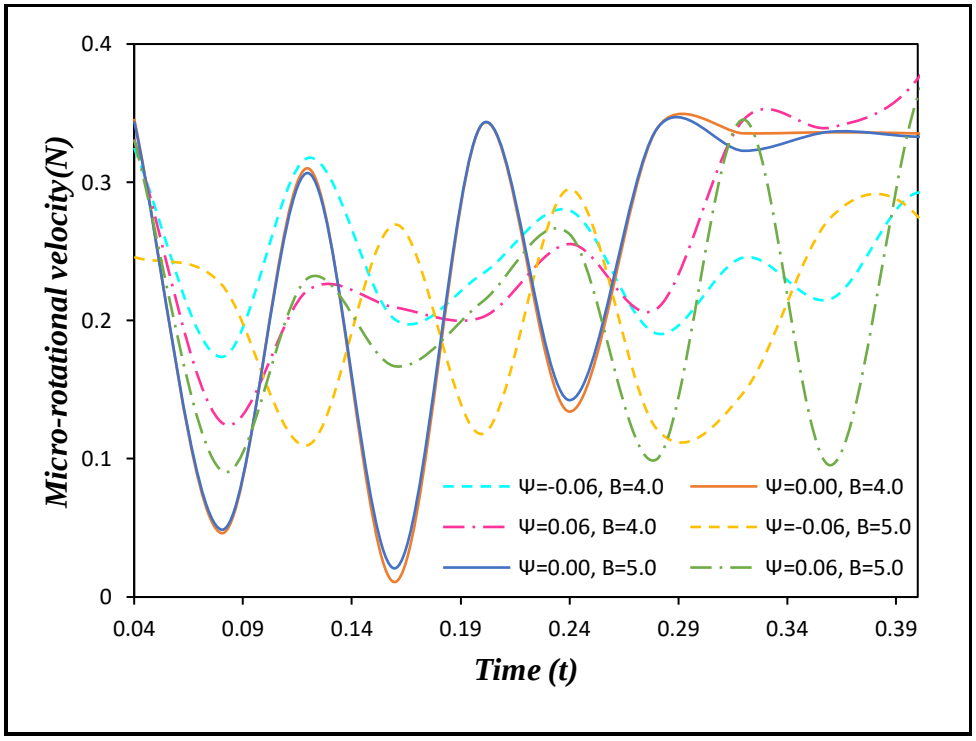

Figure 14: Effect of ***B*** on micro-rotational velocity profile for Gold (Au), $z = 1.10, \delta = 0.310, \Pr = 25,$ $r = 0.100, \alpha = 2.0, e = 1.0$

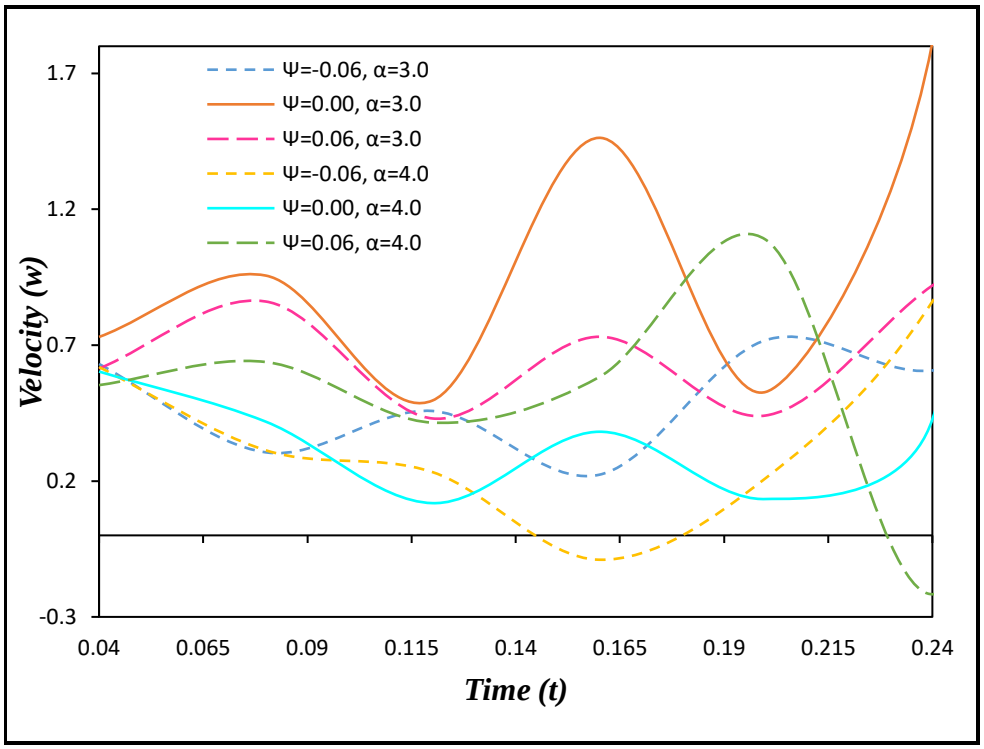

Figure 15: Effect of α on velocity profile for Gold (Au), $z = 1.10, \delta = 0.310, r = 0.100, B = 4.0, e = 1.0$

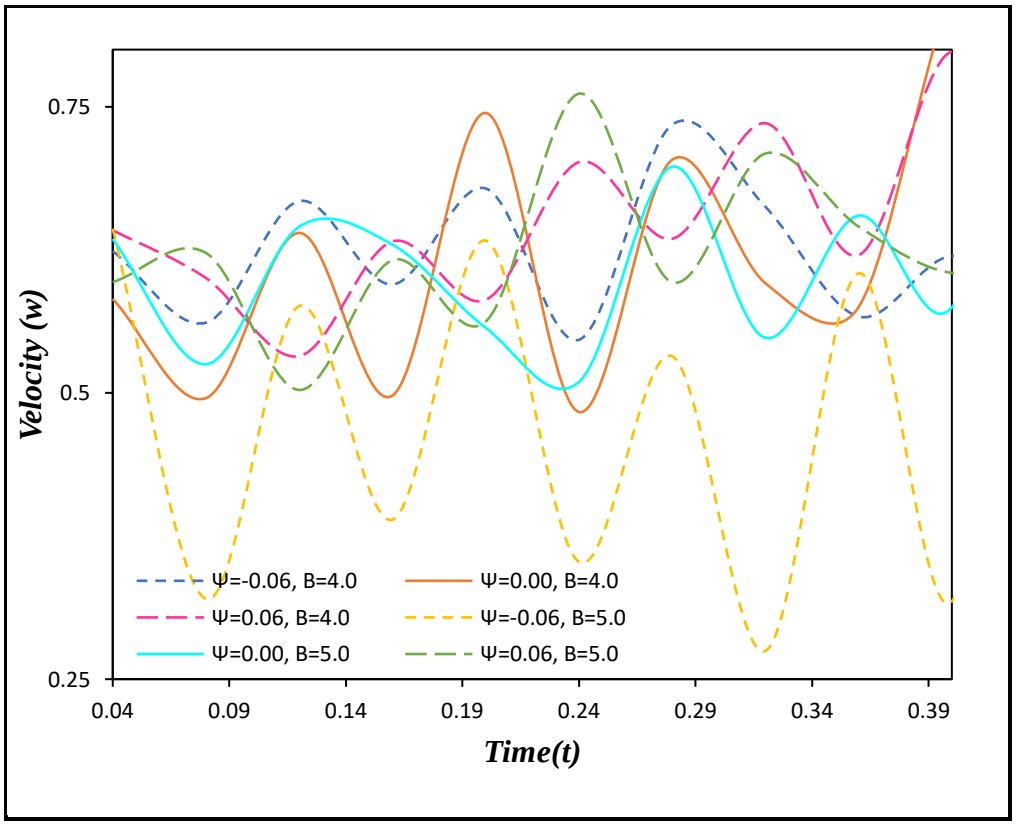

Figure 16: Effect of B on velocity profile for Gold (Au), $z = 1.10, \delta = 0.310, r = 0.100, \alpha = 2.0, e = 1.0$

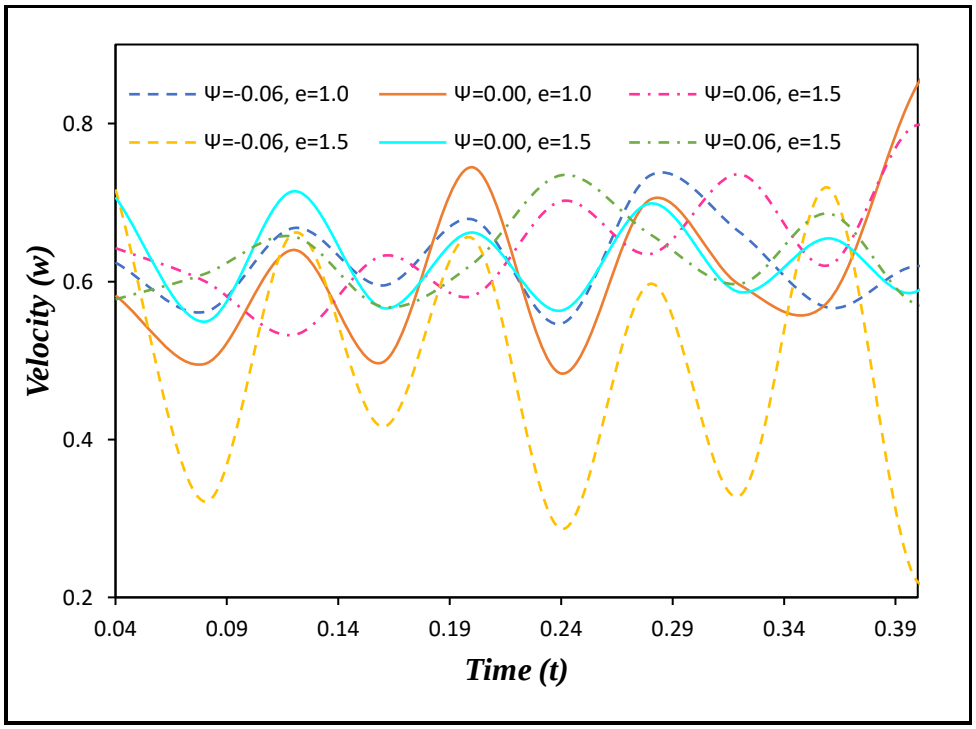

Figure 17: Effect of ***e*** on velocity profile for Gold (Au), $z = 1.10, \delta = 0.310, k = 0.1, r = 0.100,$ $B = 4.0, \alpha = 2.0$.

Table 5, documents the wall shear stress (WSS) over time (t) and indicates that an increase in the value of pulsatile constants (***B*** and ***e***), *decreases* the wall shear stress and also the WSS decreases with the a reduction in micropolar vortex viscosity, k.

Along with Table 5, **Tables 6 and 7** provide values for the wall shear stress (WSS) for various different parameters with prescribed values of Prandtl number (Pr = 14), time period (t = 0.08) at the throat of the stenosis for the two tapering angles i.e., ($\psi = 0.0592882$ *and* $\psi = -0.0592880$). The documented data indicates that in the diverging tapering case, an *increase* in nanoparticle volumetric concentration *decreases* the wall shear stress.

Table 5: *The temporal variation in wall shear stress for Gold (Au) nanoparticles*

Time (t)	*Pr=7, ϕ=0.5, Ψ = 0.06, r = 0.100 and z = 1.10*		
	α = 2.0, k = 0.3, B = 1.0, e = 0.5	*α = 2.0, k = 0.1, B = 1.0, e = 0.5*	*α = 2.0, k = 0.3, B = 2.0, e = 1.0*
0.04	0.17808	0.22246	0.17905
0.08	0.6857	0.14011	0.011724
0.12	0.29016	0.10159	0.31973
0.16	0.34412	0.46108	0.30686

0.20	0.26788	0.29359	0.29169
0.24	0.93148	0.10665	0.23813
0.28	0.75678	0.097939	0.2868
0.32	0.71857	0.17131	0.08507
0.36	0.78451	0.10707	0.30489
0.40	0.58848	0.44031	0.61399
0.44	0.80644	0.35926	0.3226
0.48	0.48670	0.011966	0.48154
0.52	0.81228	0.39076	0.34759

Table 6: *Numerical values of wall shear stress for different physical parameters at stenosis for a diverging tapering artery.*

Pr=14, Ψ = 0.06, r = 0.250 and z = 1.10					
ϕ	**α**	**B**	**e**	**k**	**WSS**
0.01	1.0	1.0	0.5	0.1	3.2837
		1.5	1.0	0.2	4.0633
0.03			1.0		3.8307
	2.0	2.0		0.2	4.0957
0.05				0.3	3.4184
0.1	2.0				4.718
	3.0	3.0	1.5	0.3	3.9179
0.3			2.0		2.7622
	3.0	3.0			1.4589
0.4	4.0	4.0		0.4	1.8649
			2.0		1.0381
0.5	5.0	5.0	2.5	0.5	1.3863

Table 7: *Numerical values of wall shear stress for different physical parameters at stenosis for a converging tapering artery.*

Pr=14, Ψ = -0.06, r = 0.190 and z = 1.10					
ϕ	**α**	**B**	**e**	**k**	**WSS**

0.01	1	1	0.5	0.1	3.0308
0.02		1.5		0.2	2.6103
			1.0		0.10599
0.04	2	2		0.2	0.83586
	2		1.0		0.36912
0.1	3	2		0.3	0.78861
			2.0	0.3	1.9925
0.3	3	3			0.90555
0.4	4		1.5		1.0988
		4		0.4	1.3622
			2.0		1.549
0.5	5	5	2.5	0.5	1.4269

5.4 Effect of Volumetric Fraction (ϕ)

Figure 18 – 21 display contour plots for micro-rotational velocity for different nanoparticle volumetric fraction (ϕ) with variation in time (t). In figure 18(a) to 18(e), it can be seen from the colored contours that with time progression, the micro-rotational velocity is damped, and the frequency of oscillations reduces with an increment in time. The figures 19 -21 shows the similar behaviour as figure 18, i.e., the frequency of oscillations reduces with increasing time; however it is also noted that by increasing the volumetric fraction (ϕ) the oscillations reduce within the arterial segment and simultaneously there is a dramatic elevation in values of micro-rotational velocity, i.e., greater doping of metallic nanoparticles (pharmacological agent) in the blood flow encourages the spin of microelements (red blood cells, etc.).

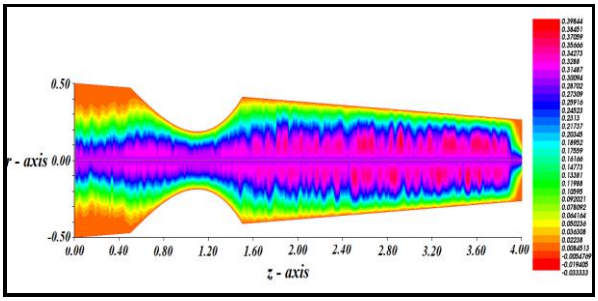

18(a)

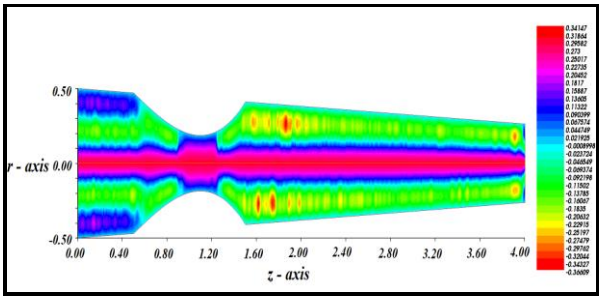

18(b)

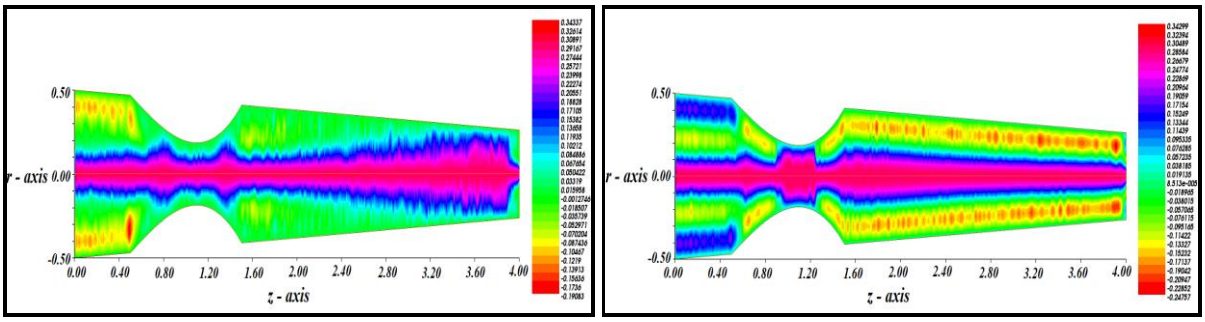

18(c) 18(d)

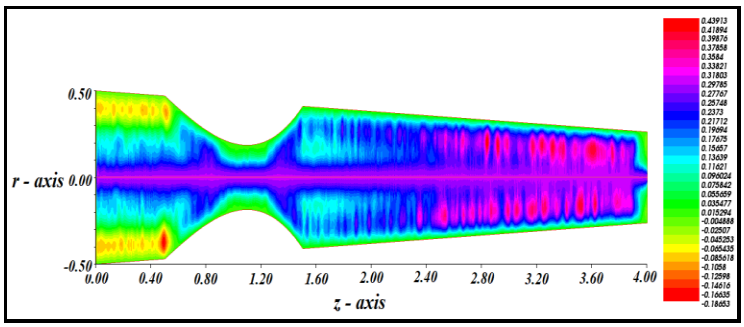

18(e)

Figure 18: Micro-rotational velocity profile for *Gold (Au) when* $\psi = -0.06, \phi = 0.01, \Pr = 25$ at $(a)\, t = 0.04,\ (b)\, t = 0.08,\ (c)\, t = 0.12,\ (d)\, t = 0.16,\ (e)\, t = 0.2$

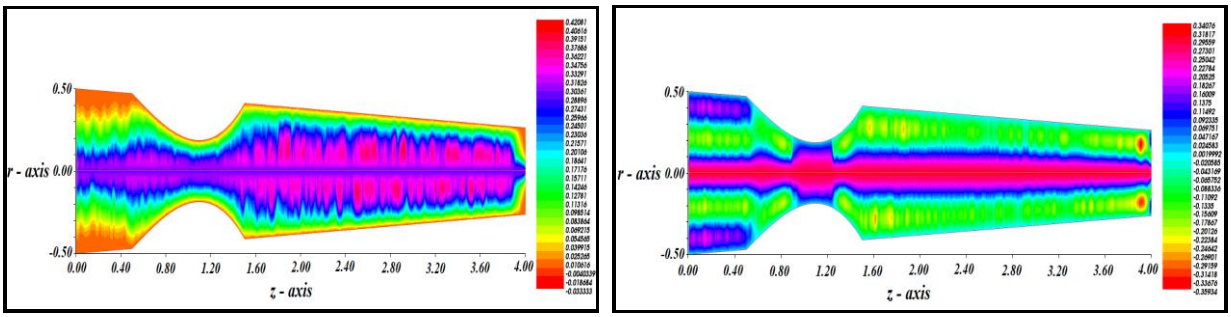

19(a) 19(b)

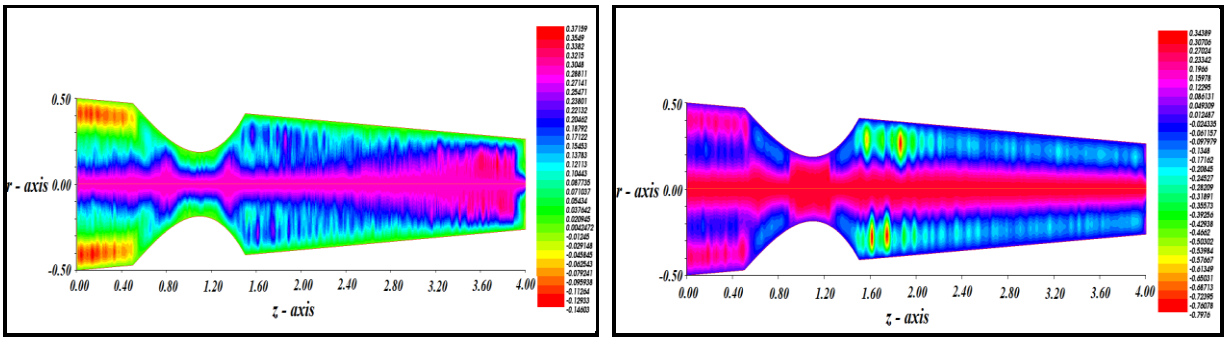

19(c) 19(d)

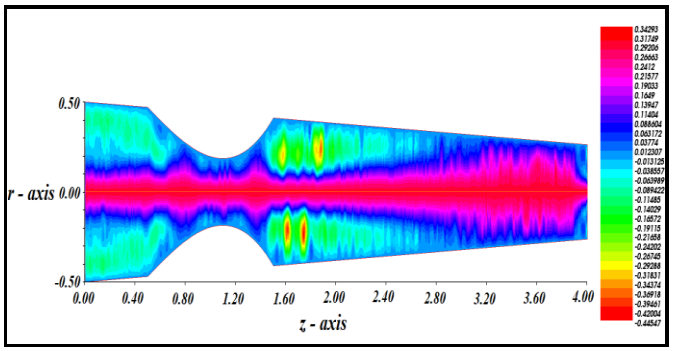

19(e)

Figure 19: Micro-rotational velocity profile for *Gold (Au) when* $\psi = -0.06, \phi = 0.02, \mathrm{Pr} = 25$ at $(a)\, t = 0.04,\ (b)\, t = 0.08,\ (c)\, t = 0.12,\ (d)\, t = 0.16,\ (e)\, t = 0.2$

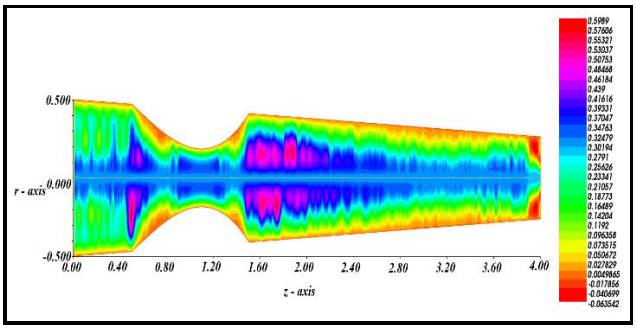

20(a)

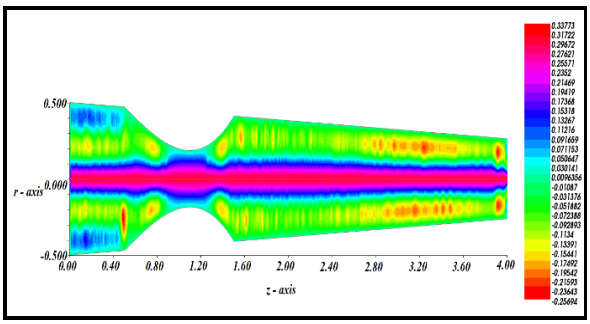

20(b)

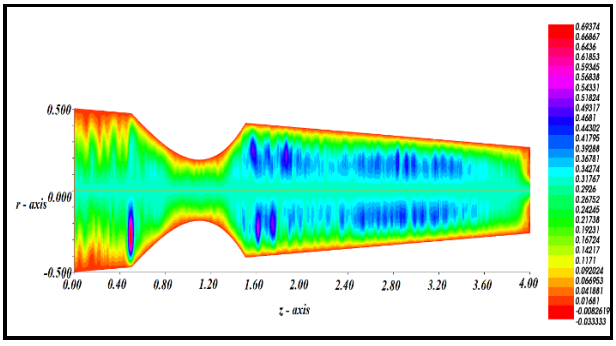

20(c)

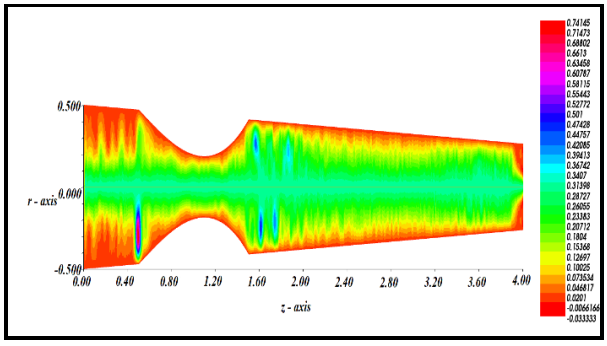

20(d)

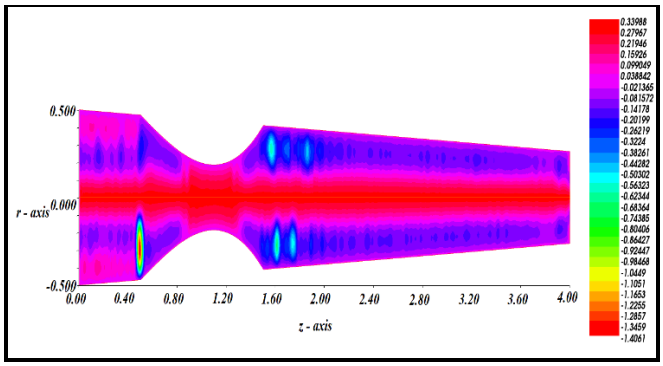

20(e)

Figure 20: Micro-rotational velocity profile for *Gold (Au) when* $\psi = -0.06, \phi = 0.1, \mathrm{Pr} = 25$ at $(a)\, t = 0.04,\ (b)\, t = 0.08,\ (c)\, t = 0.12,\ (d)\, t = 0.16,\ (e)\, t = 0.2$

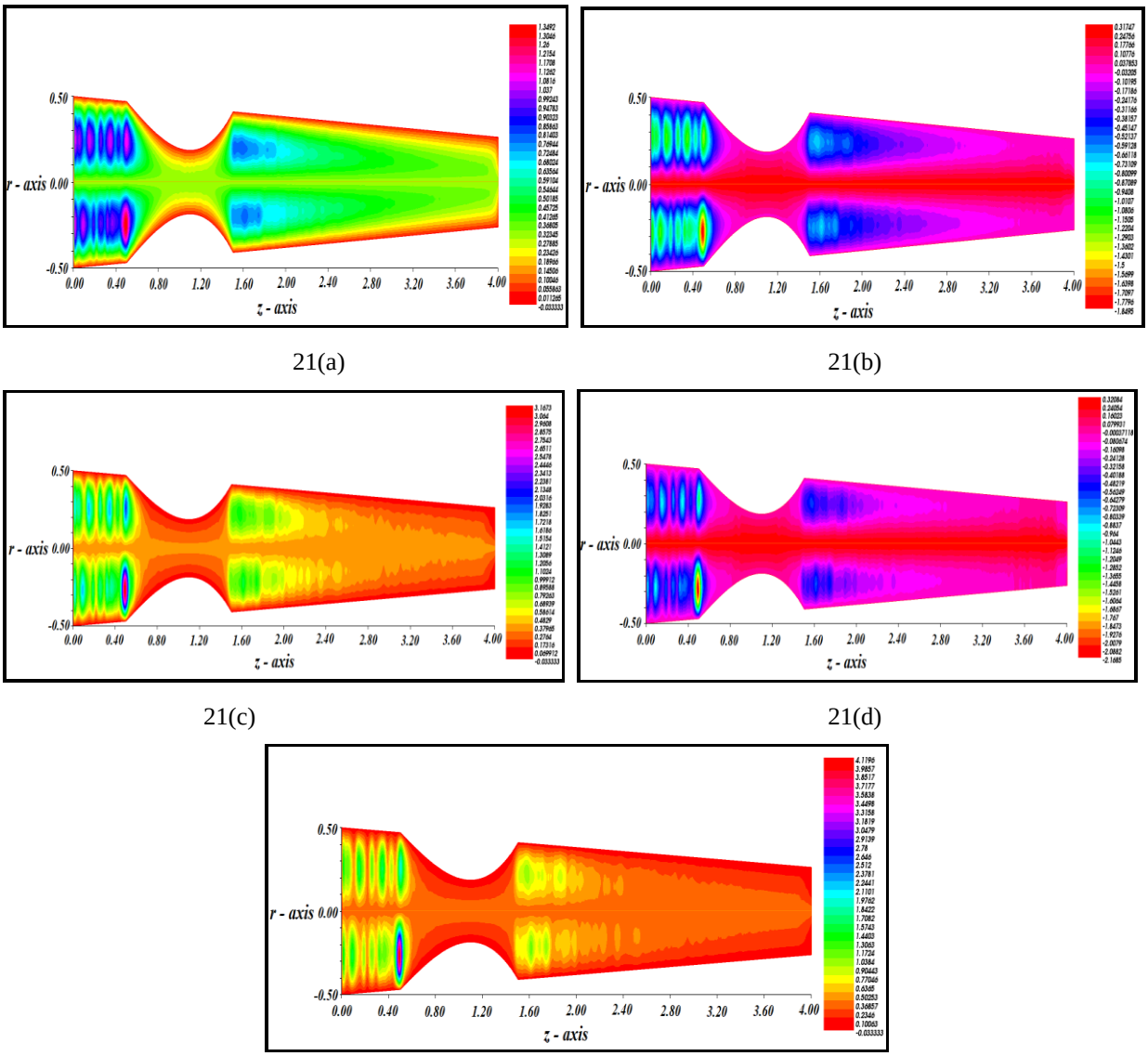

21(a) 21(b)

21(c) 21(d)

21(e)

Figure 21: Micro-rotational velocity profile for *Gold (Au) when* $\psi = -0.06, \phi = 0.3, \Pr = 25$ at $(a)\, t = 0.04,\ (b)\, t = 0.08,\ (c)\, t = 0.12,\ (d)\, t = 0.16,\ (e)\, t = 0.2$

Table 6 shows the axial variation of micro-rotational velocity (*N*) of the blood with time in the *diverging tapering arterial segment*; evidently, the value of *N* is accentuated with an increment of time in the whole artery which contrasts with the trends in figures 18 – 21 for a *converging tapering artery*. Clearly the geometric nature of the vessel location exerts a pronounced influence on the micro-rotational field, again emphasizing the need for microstructural fluid mechanics models in hemodynamics. These features simply cannot be simulated with conventional Newtonian or non-Newtonian models.

Table 8: *The axial variation in micro-rotational velocity for Gold (Au) nanoparticles at different times with* $\psi = 0.0590882,\ \alpha = 2.0, B = 4.0,\ e = 1.0,\ \phi = 0.1, z = 1.10$ *and* $r = 0.250$

z - axis	t = 0.08	t = 0.16	t = 0.24
0.00	-0.0070859	-0.013229	-0.07625
0.20	-0.0033802	-0.057766	-0.01258
0.40	-0.033802	-0.013229	-0.01258
0.60	-0.033802	-0.013229	-0.01258
0.80	-0.11395	-0.057766	0.07625
1.00	-0.060518	-0.031307	0.07625
1.20	-0.87233	-0.013229	0.07625
1.40	-0.060518	-0.013229	-0.01258
1.60	-0.24753	-0.5922	-0.72703
1.80	-0.274241	-0.50313	-0.90564
2.00	-0.22081	-0.41405	-0.45911
2.20	-0.32768	-0.5922	-0.90564
2.40	-0.30096	-0.63674	-0.90564
2.60	-0.32768	-0.72581	-0.90564
2.80	-0.274241	-0.41405	-0.63772
3.00	-0.30096	-0.50313	-0.72703
3.20	-0.30096	-0.41405	-0.63772
3.40	-0.22801	-0.32498	-0.3698
3.60	-0.24753	-0.32498	-0.45911
3.80	-0.060518	-0.057766	-0.10189
4.00	-0.033802	-0.013229	-0.01258

5.5 Effect of tapering angle (ψ)

Figure 22 captures the strongly pulsatile nature of linear (translational) velocity profile and features three tapering angle cases with respect to time. At the centre line of the artery (core zone), the velocity is low for the non-tapered artery compared to the diverging and converging cases. However, it *increases gradually* with progress in time, and after a specific time, very prominent acceleration in the linear flow is observed i.e., the rapid ascent in velocity.

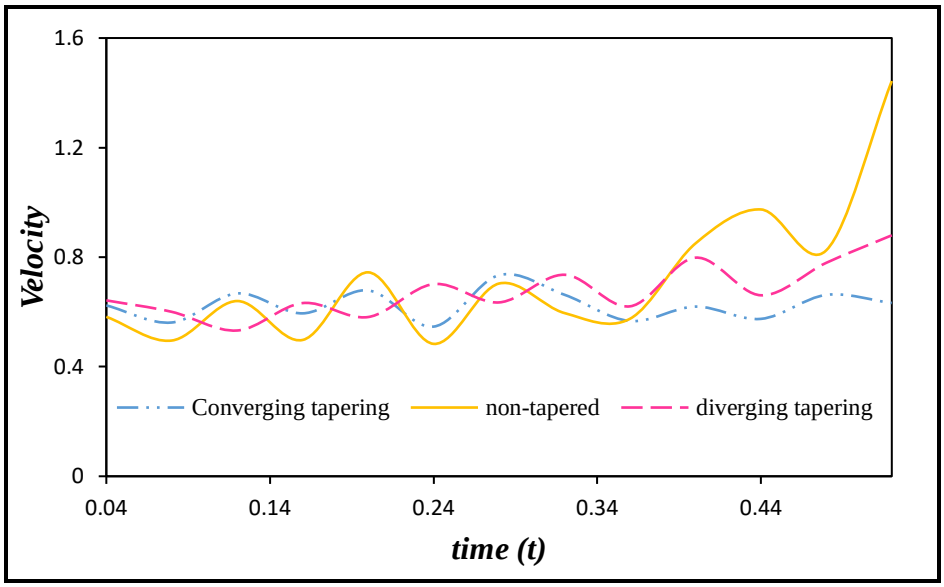

Figure 22: Effect of ψ on velocity profile for $Gold(Au), r = 0.10, \Pr = 25, z = 1.10, \phi = 0.1$

Figures 23, 24 visualize the micro-rotation velocity variation with time again for three tapering angles and at two different axial locations. Micro-rotation topology is similar to the linear velocity profile (figure 22). The micro-rotation (angular velocity of microelements) for *the non-tapered artery* shows a marked increment initially and exhibits a significant decrement after a specific time.

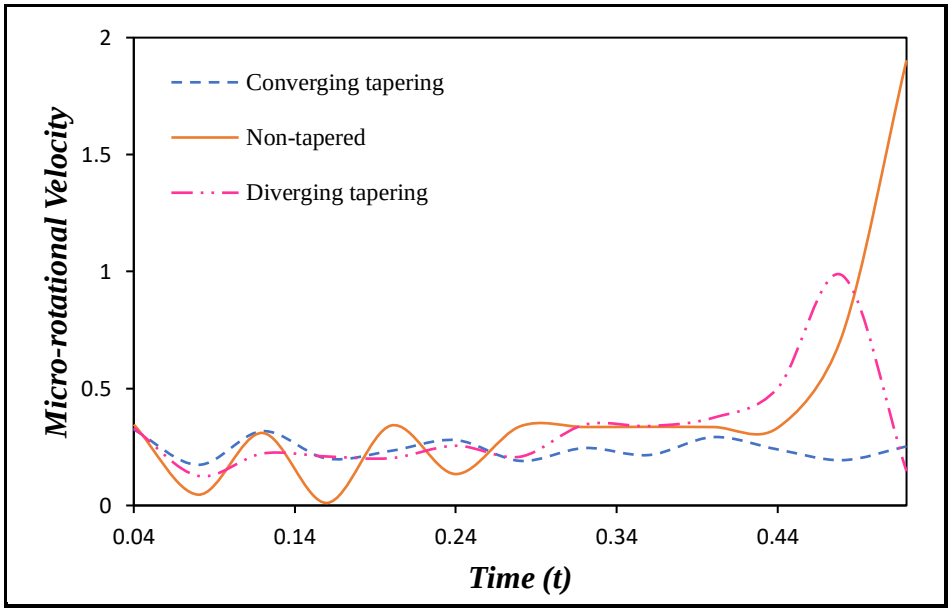

Figure 23: Effect of ψ on micro-rotational velocity for $Gold(Au), r = 0.10, \Pr = 25, z = 1.10, \phi = 0.1$

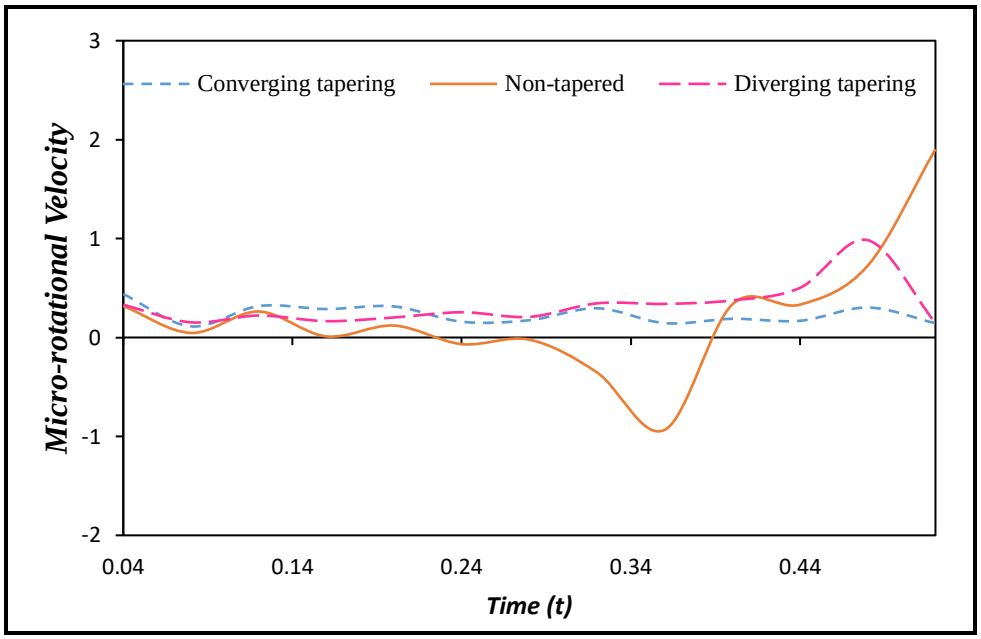

Figure 24: Effect of ψ on micro-rotational velocity profile for $Gold(Au), r = 0.10, \Pr = 25, z = 0.5, \phi = 0.1$

Figures 25-27 display the volumetric flow rate over time (t) at different radial locations.

Figure 25 shows that in the case of a *converging tapering artery*, the flow rate is more pulsatile in nature. Figures 26 and 27 demonstrate that the volumetric flow rate is enhanced as we progress forward from the centreline of the artery to the arterial wall.

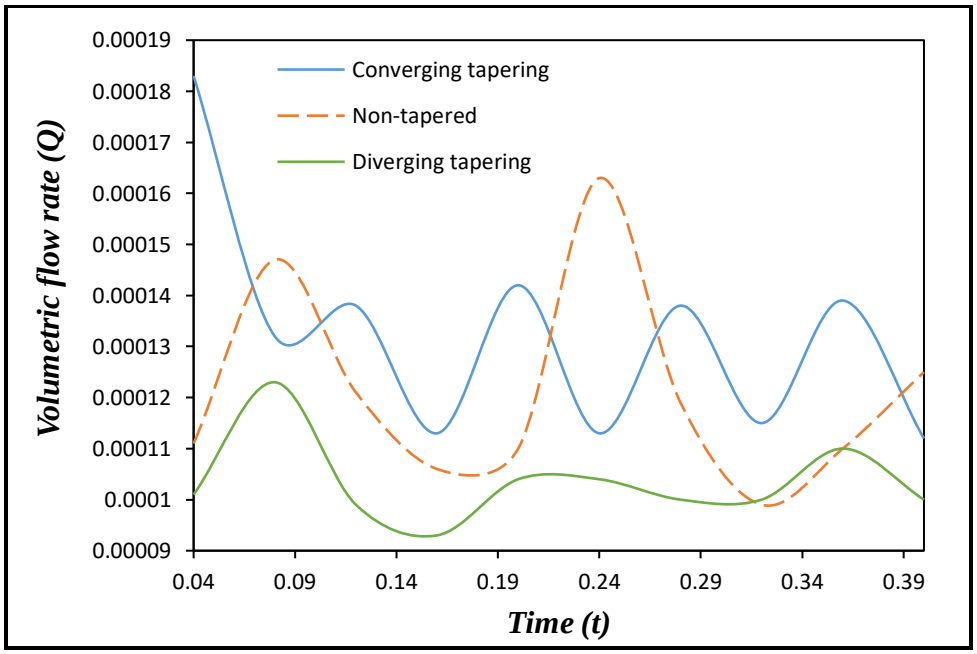

Figure 25: Volumetric flow rate (Q) for $Gold(Au), r = 0.025, B = 2.0, \alpha = 2.0, e = 1.0, k = 0.3, \Pr = 14,$ $z = 1.10, \phi = 0.5$

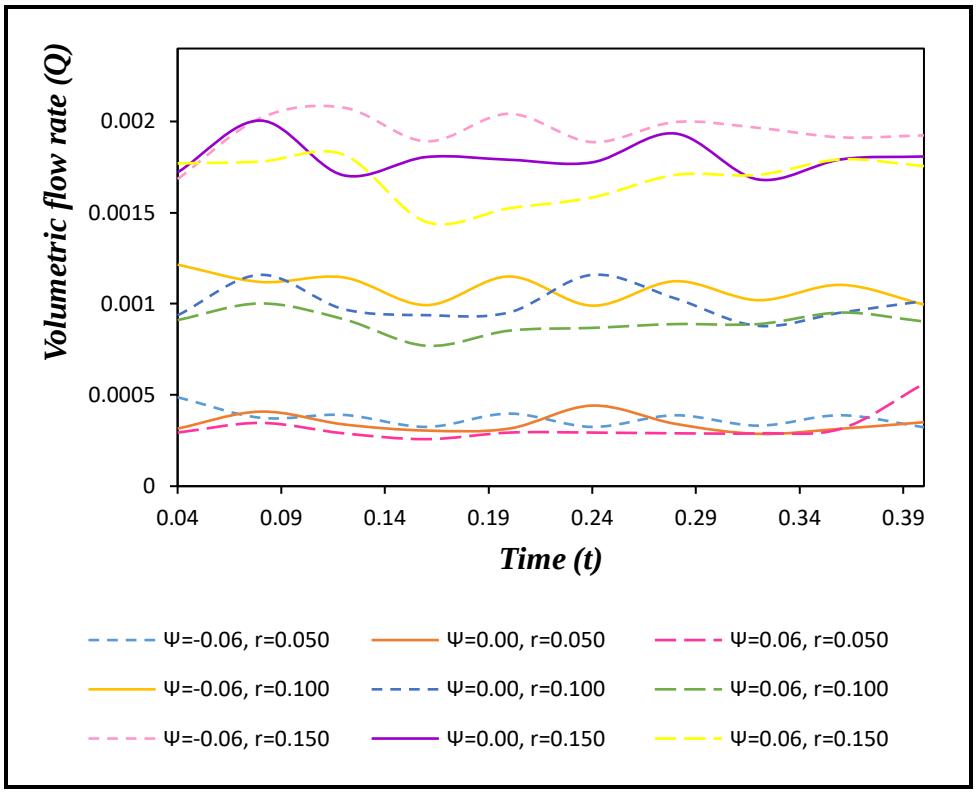

Figure 26: Volumetric flow rate (Q) for

$Gold(Au), B = 2.0, \alpha = 2.0, e = 1.0, k = 0.3, \Pr = 14, z = 1.10, \phi = 0.5$

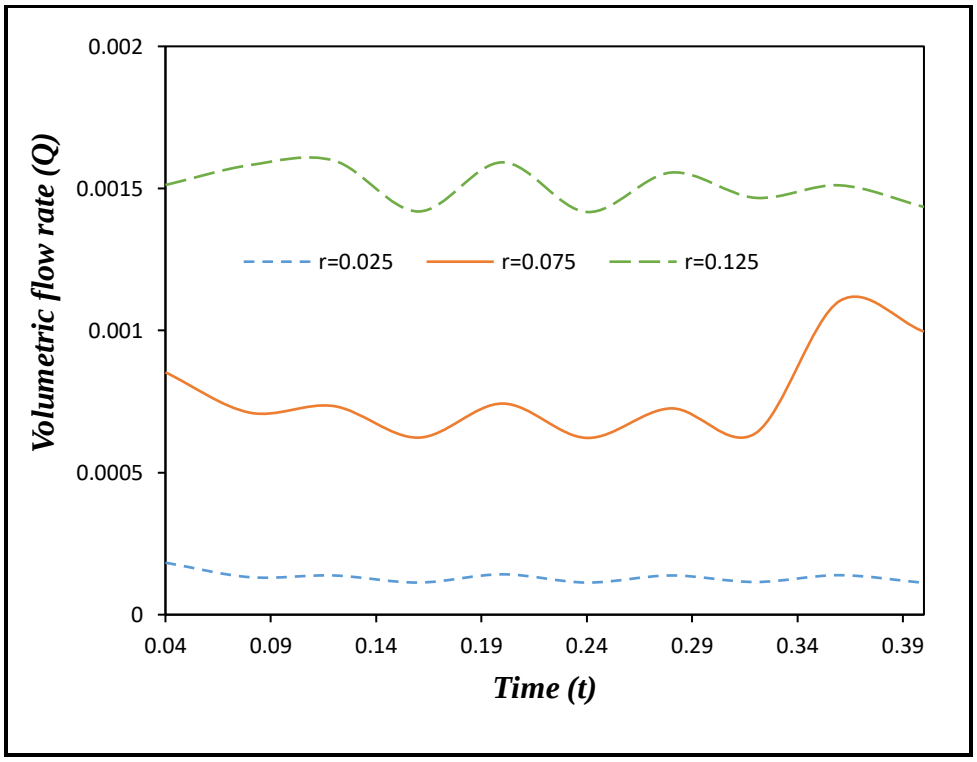

Figure 27: Volumetric flow rate (Q) for $Gold(Au), \psi = 0.06, B = 2.0, \alpha = 2.0, e = 1.0, k = 0.3,$

$\Pr = 14, z = 1.10, \phi = 0.5$

Finally, **Fig. 28** presents the effect of tapering angles on hemodynamic impedance, which is initially high but gradually decreases with time progression for the *converging tapering case* (since this achieves a higher volumetric flow rate).

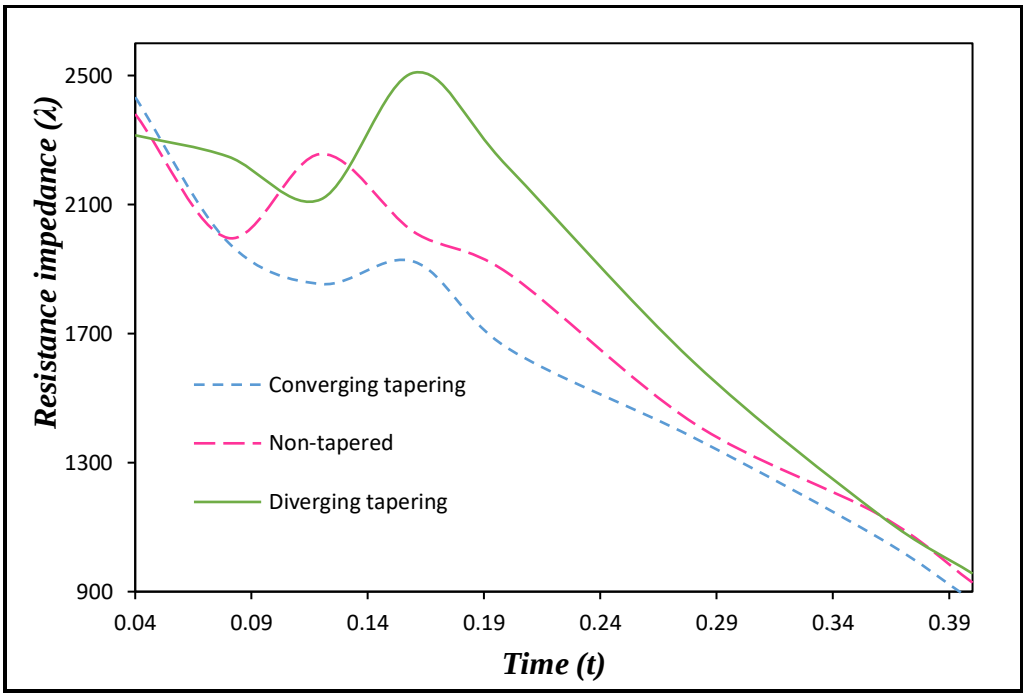

Figure 28: Volumetric flow rate (Q) for $Gold(Au), r = 0.150, B = 2.0, \alpha = 2.0, e = 1.0, k = 0.3,$ $Pr = 14, z = 1.10, \phi = 0.5.$

6. STATISTICAL PARADIGM

In this section, we have extended the study to investigate the relative influence of different parameters on transport characteristics with the priority being to understand the relation between the various physical parameter and wall shear stress. We have already reported the values of wall shear stress for different tapering artery in **Tables 6 and 7**. The values of correlation coefficients are calculated for both of the above-mentioned cases in **Tables 9 and 10** respectively. In the statistical analysis, to, for example, determine the significant correlation between the variables and p-value, we considered the value of the significance level as $\lambda = 0.05$. The *correlation coefficient*, *cc*, is defined as:

$$cc = \frac{Cov(x, y)}{\sigma_x * \sigma_y} \tag{34}$$

Here $Cov(x, y)$ = Covariance of the two variables *x and y*, σ_x = Standard deviation of variable *x* and σ_y = Standard deviation of variable y.

For the *p-value calculation*, we first define the following relation:

$$t' = cc\sqrt{n-2} \Big/ \sqrt{1-cc^2} \tag{35}$$

Finally, the *p-value* is calculated as the corresponding two-sided *p*-value for the *t*-distribution with *n-2* degrees of freedom using the relation:

$$p-value = t-dist\_2t(t', n-2). \tag{36}$$

Here ***cc*** = correlation coefficient, *n* = sample size and t' = t-score.

The value of correlation coefficient (***cc***) lies between -1 and 1. It is not only employed to explore the relation between two variants but also used to reveal the inverse and direct correspondence between those variants. For the statistical analysis, the correlation coefficient has following interpretations:

- If ***cc*** = 1, then there is a perfect positive linear relationship between the two variables.
- If $\pm 0.80 \le cc \le \pm 0.999$, then there is a very strong positive (negative) linear relationship between the two variables.
- If $\pm 0.60 \le cc \le \pm 0.799$, then there is a strong positive (negative) linear relationship between the two variables.
- If $\pm 0.40 \le cc \le \pm 0.599$, then there is a moderate positive (negative) linear relationship between the two variables.
- If $\pm 0.20 \le cc \le \pm 0.399$, then there is a weak positive (negative) linear relationship between the two variables.
- If $0.00 \le cc \le \pm 0.199$, then there is a very weak positive (negative) linear relationship between the two variables.
- If ***cc*** = 0, then there is no linear relationship between the two variables.
- If ***cc*** = -1, then there is a perfect negative linear relationship between the two variables.

Table 9: Correlation coefficient between wall shear stress and selected physical parameters at stenosis for a diverging tapering artery when *Pr=14, Ψ = 0.06, r = 0.250 and z = 1.10*

Parameter	***Correlation coefficient (cc)***	***p-value***
ϕ	-0.85342	0.01 (< λ)
α	-0.70167	0.08 (> λ)
B	-0.73853	0.06 (> λ)

e	-0.75160	0.05 (= λ)
k	-0.78677	0.03 (< λ)

Table 10: Correlation coefficient between wall shear stress and selected physical parameters at stenosis for a converging tapering artery when *Pr=14, Ψ = -0.06, r = 0.190 and z = 1.10*

Parameter	***Correlation coefficient (cc)***	***p-value***
ϕ	-0.42764	0.3 (> λ)
α	-0.30156	0.5 (> λ)
B	-0.44472	0.3 (> λ)
k	-0.51386	0.2 (> λ)

From **Tables 9 and 10**, we can observe that in the case of a *diverging tapering artery*, the volume fraction (ϕ), Womersley number (α), pulsatile constant (B) and Eringen micropolar vortex viscosity material parameter (k), all exhibit a strong negative linear relationship with wall shear stress as the value of correlation coefficient (*cc*) *exceeds* 0.6. Also, it is noteworthy that in the case of a converging tapering artery, the volume fraction (ϕ), pulsatile constant (B) and Eringen micropolar vortex viscosity material parameter (k), demonstrate a moderate negative linear relationship with the wall shear stress. Based on analysing the statistically calculated *p*-value, for both converging and diverging tapered arteries, represented in **Tables 9 and 10**, it can be inferred that in the case of a diverging tapering artery, the volume fraction (ϕ), the pulsatile constant (e) and Eringen micropolar vortex viscosity material parameter (k), the p-value is less than the λ value considered i.e., the p-value < λ. Hence for these cases we have identified a significant correlation. Noting that earlier, in Table 4, validation of the present study with the published finite difference results obtained by Ali *et al.* [16] was conducted, the value of correlation coefficient (***cc***) between the adopted numerical values of FDM and simulated values by FEM has been calculated as ***cc*** = 0.996920 *with a corresponding p-value* of 7.2836E-08. Hence the given data in table 4 represents the existence of a very strong positive correlation between the two calculated velocity values. Finally, it may be noted that the p-value is much less than the considered value of λ, confirming that the computations in Table 4 show a significant positive correlation.

7. CONCLUSIONS

A novel mathematical model for axisymmetric rheological laminar hemodynamics conveying nanoparticles (pharmacological agents) through a diseased tapered artery with a mild stenosis present has been developed. Different metallic nanoparticles homogeneously suspended in the blood are considered, motivated by drug delivery (pharmacology) applications. The Eringen micropolar model has been utilized for hemorheological characteristics in the whole arterial region. The conservation equations for mass, linear momentum, angular momentum (micro-rotation), and energy and nanoparticle species are normalized by employing appropriate non-dimensional variables. The transformed equations are solved numerically subject to physically appropriate boundary conditions using the finite element method with the variational formulation scheme available in the FreeFEM++ code. A good correlation is achieved between the FreeFEM++ computations and published FDM results. The effect of selected parameters i.e., *Womersley parameter (α), pulsatile constants (B and e), Prandtl number (Pr), Eringen micropolar vortex viscosity parameter (k), volumetric fraction (ϕ)* on velocity, temperature and micro-rotational (Eringen angular) velocity, wall shear stress, volumetric flow rate and hemodynamic impedance of blood flow has been computed. Colour contours and graphs have been included to visualize the simulated blood flow characteristics. The present simulations have shown that:

- The linear velocity exhibits greater enhancement in the converging tapering and non-tapered arterial segment in comparison to a diverging tapering artery while the micro-rotational velocity shows a greater increment in the diverging tapering artery.
- The tendency of variation is more in temperature as compared to velocity and micro-rotational velocity; temperature shows a significant negative or positive transition over time with radial coordinate.
- An increment in Prandtl number decreases the micro-rotational velocity i.e., suppresses microelement (e.g., red blood cell) spin with time increment in all the tapering cases.
- The Womersley parameter shows the same effect on both linear velocity and micro-rotational velocity i.e., both are decreased.
- An increment in Eringen micropolar vortex viscosity parameter enhances the micro-rotational velocity and amplifies the pulsatile nature of the profiles; however, at intermediate values microrotation is suppressed.
- The pulsatile constants (***B*** and **e**) have different effects on velocity, micro-rotational velocity and pressure gradient. Pressure gradient increases with the increment in ***B*** and

e. Also, the pulsatile nature of velocity and micro-rotational velocity increases with an increment of ***B*** and ***e.***

- Elevation in volumetric fraction (ϕ) damps the linear velocity oscillations within the arterial segment whereas it enhances micro-rotational velocity i.e., greater doping of metallic nanoparticles (pharmacological agent) in the blood flow encourages the spin of microelements (red blood cells etc).
- Based on statistical analysis, a significant negative strong correlation is shown to exist between the wall shear stress (WSS) and volume fraction (ϕ), Eringen micropolar vortex viscosity material parameter (k) and pulsatile constant (e) for the case of a *diverging* tapering artery.

The present study has furnished new insights into nano-doped non-Newtonian microstructural hemodynamics in stenosed tapered arteries. Future studies will consider flexibility of the arterial vessel i.e., fluid-structure interaction and will be communicated imminently.

ACKNOWLEDGEMENTS

The authors are grateful to the Science and Engineering Research Board (SERB), Department of Science and Technology (DST), government of India for undertaking the research work under the research project File Number: ECR/2017/001053 dated 12/03/2018.

REFERENCES

[1] R Skalak, S R Keller, T W Secomb, Mechanics of blood flow**,** *ASME J. Biomech Eng*, 103(2):102-15 (1981).

[2] Tu, Jiyuan, Inthavong, Kiao, Wong, Kelvin Kian Loong *Computational Hemodynamics – Theory, Modelling and Applications*, Springer, Netherlands (2016).

[3] Karimipour, A., Toghraie, D., Abdulkareem, L. A., Alizadeh, A. A., Zarringhalam, M., & Karimipour, A. (2020). Roll of stenosis severity, artery radius and blood fluid behavior on the flow velocity in the arteries: *Application in Biomedical Engineering. Medical Hypotheses*, 109864.

[4] Amiri, M. H., Keshavarzi, A., Karimipour, A., Bahiraei, M., Goodarzi, M., & Esfahani, J. A. (2019). A 3-D numerical simulation of non-Newtonian blood flow through femoral artery bifurcation with a moderate arteriosclerosis: investigating Newtonian/non-Newtonian flow and its effects on elastic vessel walls. *Heat and Mass Transfer*, 55(7), 2037-2047.

[5] Padma, R., Ponalagusamy, R., & Selvi, R. T. (2019). Mathematical modeling of electro hydrodynamic non-Newtonian fluid flow through tapered arterial stenosis with periodic body acceleration and applied magnetic field. *Applied Mathematics and Computation*, 362, 124453.

[6] Agrawal V, Paul C, Das M K and Muralidhar K (2015) Effect of coil embolization on blood flow through a saccular cerebral aneurysm. *Sadhana* 40(3): 875–887.

[7] Priyadharshini S and Ponalagusamy R 2017 Computational model on pulsatile flow of blood through a tapered arterial stenosis with radially variable viscosity and magnetic field. *Sadhana*, 42(11): 1901–1913.

[8] B. V. R. Kumar and K. B. Naidu, "Finite element analysis of nonlinear pulsatile suspension flow dynamics in blood vessels with aneurysm", *Comp. Biol. Med*., vol. 25, pp 1-20, 1995.

[9] Haghighi, A. R., & Chalak, S. A., Mathematical modelling of blood flow through a stenosed artery under body acceleration. *J. Brazilian Society of Mechanical Sciences and Engineering*, **39**(7), 2487-2494, 2017.

[10] Gupta, Rajeev, Indu Mohan, and Jagat Narula. "Trends in coronary heart disease epidemiology in India." *Annals of Global Health* 82, no. 2 (2016): 307-315.

[11] Chakravarty, S., & Mandal, P. K. (1994). Mathematical modelling of blood flow through an overlapping arterial stenosis. *Mathematical and Computer Modelling*, 19(1), 59-70.

[12] Anand M, Rajagopal KR (2004) A shear-thinning viscoelastic fluid model for describing the flow of blood. *Int J Cardiovasc Med Sci* 4(2):59–68.

[13] Mandal, PK. (2005). "An unsteady analysis of non-Newtonian blood flow through tapered arteries with a stenosis", *International Journal of Non-Linear Mechanics*. **40**. 151-164.

[14] Chakravarty, Santabrata, and Prashanta Kumar Mandal. "Numerical simulation of Casson fluid flow through differently shaped arterial stenoses." *Zeitschrift für angewandte Mathematik und Physik* 65, no. 4 (2014): 767-782.

[15] Ali, N., Zaman A., Sajid M., Bég, Anwar O., Shamshuddin M. D. and Ali Kadir (2018), Numerical simulation of time-dependent non-Newtonian nano-pharmacodynamic transport phenomena in a tapered overlapping stenosed artery, *Nanoscience and Technology: An International Journal*, **9**, 247-282.

[16] Cokelet G.R., (1972), The rheology of human blood. In: *Fung Y.C. (ed) Biomechanics- its foundations and objectives,* Prentice Hall, New York.

[17] Shibeshi, S. S., & Collins, W. E. (2005). The rheology of blood flow in a branched arterial system. *Applied Rheology*, 15(6), 398-405.

[18] Amiri, M. H., Keshavarzi, A., Karimipour, A., Bahiraei, M., Goodarzi, M., & Esfahani, J. A. (2019). A 3-D numerical simulation of non-Newtonian blood flow through femoral artery bifurcation with a moderate arteriosclerosis: investigating Newtonian/non-Newtonian flow and its effects on elastic vessel walls. *Heat and Mass Transfer*, 55(7), 2037-2047.

[19] Jamalabadi, M. Y. A., Daqiqshirazi, M., Nasiri, H., Safaei, M. R., & Nguyen, T. K. (2018). Modeling and analysis of biomagnetic blood Carreau fluid flow through a stenosis artery with magnetic heat transfer: A transient study. *PloS one*, 13(2).

[20] Shabbir, M. S., Ali, N., & Abbas, Z. (2018). Unsteady blood flow of non-Newtonian fluid through a rigid artery in the presence of multi-irregular stenoses. *Journal of the Brazilian Society of Mechanical Sciences and Engineering*, 40(9), 413.

[22] Ponalagusamy, R., & Manchi, R. (2019). A four-layered model for flow of non-Newtonian fluid in an artery with mild stenosis. Sādhanā, 44(7), 158.

[22] Tzirakisa, K. Botti, L. Vavourakis, V. and Papaharilaou, Y. (2016), Numerical modelling of non-Newtonian biomagnetic fluid flow, *Computers and Fluids* **126**. 170–180.

[23] Nadeem, S. and Akbar, NS. (2009). "Influence of heat transfer on peristaltic transport of Herschel–Bulkley fluid in a non-uniform inclined tube", *Communications in Nonlinear Science and Numerical Simulation*. **14**. 4100-4113.

[24] Nadeem, S., Akbar, NS., Hendi, AA. and Hayat, T. (2011). "Power law fluid model for blood flow through a tapered artery with stenosis", *Applied Mathematics and Computation*. **217**. 7108-7116.

[25] Mekheimer, KS. and El kot, MA. (2012). Mathematical modelling of unsteady flow of a Sisko fluid through an anisotropically tapered elastic arteries with time-variant overlapping stenosis. *Applied Mathematical Modelling*. **36**. 5393-5407.

[26] A.C. Eringen (1966) Theory of micropolar fluids. *USSR J. Math Mech* 16(1):909–923.

[27] "Mechanics of Micromorphie Continua", *Mechanics of Generalized Continua* (Ed. E. Kröner), Springer-Verlag, Germany, pp. 18–35 (1967).

[28] A.C. Eringen, *Microcontinuum Field Theories II: Fluent Media*, Springer, New York (2001).

[29] T. Ariman, On the analysis of blood flow, *J. Biomechanics***, 4 (3)** 185-192 (1971).

[30] C.K. Kang A.C. Eringen, "The effect of microstructure on the rheological properties of blood", *Bulletin of Mathematical Biology*, *38,* 135–159 (1976).

[31] Wayland, H. 1967. "Rheology and the Microcirculation", *Gastroenterology*,**52**, 342–355.

[32] Oguz K. Baskurt, Max R. Hardeman, Michael W. Rampling, Herbert J. Meiselman *Handbook of Hemorheology and Hemodynamics*, IOS Press, USA (2007).

[33] Cowin, S. C. 1972. "On the polar fluid as a model for blood flow in tubes."*Biorheology*, **9**, 23–25.

[34] H. Ramkissoon and S. R. Majumdar, "Drag on an axially symmetric body in the Stokes' flow of micropolar fluid," *Phys. Fluids* **19**, 16–21 (1976).

[35] P. Chaturani and V. S. Upadhya, "On micropolar fluid model for blood flow through narrow tubes," Biorheology **16**, 419–428 (1979).

[36] O. Anwar Bég, H.S. Takhar, R. Bhargava, S. Sharma and T-K Hung, "Mathematical modeling of biomagnetic flow in a micropolar fluid-saturated Darcian porous medium", *Int. J. Fluid Mechanics Research*, 34, 5, 403-424 (2007).

[37] R. Bhargava, S. Sharma, O. Anwar Bég and Zueco, J, "Finite element study of nonlinear two-dimensional deoxygenated biomagnetic micropolar flow", *Communications in Nonlinear Science and Numerical Simulation Journal*, 15, 1210-1233 (2010).

[38] KucabaPiętal A.: *Microflows Modelling based on Micropolar Fluid Theory*, The Printing House of The Rzeszów University of Technology, Rzeszów (2004).

[39] O. Anwar Bég, M.M. Rashidi, T. A. Bég and M. Asadi, "Homotopy analysis of transient magneto-bio-fluid dynamics of micropolar squeeze film: *a model for magneto-bio-rheological lubrication*", *J. Mechanics In Medicine and Biology*, 12, 3, 1250051-1 to 1250051-21, (2012).

[40] G. Ravi Kiran, G. Radhakrishnamacharya and O. Anwar Bég, "Peristaltic flow and hydrodynamic dispersion of a reactive micropolar fluid: simulation of chemical effects in the digestive process", *J. Mechanics in Medicine and Biology*, 17, 1750013 (2017). [17 pages]

[41] Jean-François Ganghoffer and Ibrahim Goda, Chapter 6 - Micropolar Models of Trabecular Bone, In *Multiscale Biomechanics*, 263-316 (2018).

[42] N. Ali, Z. Asghar and O. Anwar Bég, "A mathematical model of bacterial gliding on a thin layer of micropolar slime", *Results in Physics (Netherlands)*, 9, 682-691 (2018).

[43] D.Yu., Khanukaev, A.N.Filippov, P.K.Yadav, A.Tiwari, "Creeping flow of micropolar fluid through a swarm of cylindrical cells with porous layer (membrane)", *Journal of Molecular Liquids*, 294, 111558 (2019).

[44] M.K. Chaube, A. Yadav, D. Tripathi and O. Anwar Bég, "Electroosmotic flow of biorheological micropolar fluids through microfluidic channels ", *Korea-Australia Rheology Journal*, 30(2), 89-98 (2018)**.**

[45] E.G.Karvelas, A.Tsiantis, T.D.Papathanasiou, "Effect of micropolar fluid properties on the hydraulic permeability of fibrous biomaterials", *Computer Methods and Programs in Biomedicine*, 185, 105135 (2020).

[46] N. S. Akbar, D. Tripathi, Z. H. Khan and O. Anwar Bég, "Mathematical modelling of pressure-driven micropolar biological flow due to metachronal wave propulsion of beating cilia", *Mathematical Biosciences*, 301, 121-128 (2018).

[47] R. Devanathan and S. Parvathamma, "Flow of micropolar fluid through a tube with stenosis," *Med. Biol. Eng. Comput*. 21, 438–445 (1983).

[48] K. S. Mekheimer and M. A. El Kot, "The micropolar fluid model for blood flow through a tapered artery with a stenosis," *Acta Mech. Sin*. **24**, 637–644 (2008).

[49] M. A. Ikbal, S. Chakravarty, and P. K. Mandal, "Two-layered micropolar fluid flow through stenosed artery: Effect of peripheral layer thickness," *Comput. Math. Appl*. **58**, 1328–1339 (2009).

[50] Samad, N. A. (2013). "Numerical solution of mass transfer to micropolar fluid flow past a stenosed artery", *PhD dissertation, Universiti Teknologi, Malaysia*.

[51] Ellahi, R., Rahman, SU., Gulzar, M., Nadeem, S., and Vafai, K. (2014). "A mathematical study of non-Newtonian micropolar fluid in arterial blood flow through composite stenosis", *Applied Mathematics & Information Sciences*. **4**. 1567–1573.

[52] Zaman, A., Ali, N., & Bég, O. Anwar (2016). "Numerical simulation of unsteady micropolar hemodynamics in a tapered catheterized artery with a combination of stenosis and aneurysm". *Medical & Biological Engineering & Computing*, 54(9), 1423-1436.

[53] Tiwari, A., Shah, P. D., & Chauhan, S. S. (2020). "Analytical study of micropolar fluid flow through porous layered micro-vessels with heat transfer approach". *The European Physical Journal Plus*, 135(2), 209.

[54] Sahoo, S. K., Parveen, S., & Panda, J. J. (2007). "The present and future of nanotechnology in human health care". *Nanomedicine: Nanotechnology, Biology and Medicine*, 3(1), 20-31.

[55] Lam P-L, Wong W-Y, Bian Z, Chui C-H, Gambari R. "Recent advances in green nanoparticulate systems for drug delivery: efficient delivery and safety concern". *Nanomedicine*. 2017; 12:357–85.

[56] Martín Giménez, V. M., Kassuha, D. E., &Manucha, W. (2017). "Nanomedicine applied to cardiovascular diseases: latest developments ". *Therapeutic Advances in Cardiovascular Disease*, 11(4), 133-142.

[57] Junyaprasert VB, Morakul B. "Nanocrystals for enhancement of oral bioavailability of poorly water-soluble drugs". *Asian J Pharm Sci*. 2015; 10:13–23.

[58] N. S. Akbar, D. Tripathi and O. Anwar Bég, "Variable-viscosity thermal hemodynamic slip flow conveying nanoparticles through a permeable-walled composite stenosed artery", *European Physical Journal Plus*, 132: 294 -305 (2017).

[59] Ijaz, S., & Nadeem, S. (2018). "Consequences of blood mediated nano transportation as drug agent to attenuate the atherosclerotic lesions with permeability impacts". *Journal of Molecular Liquids*, 262, 565-575.

[60] Tripathi, D. and Bég, O. Anwar., "A study on peristaltic flow of nanofluids: application in drug delivery systems", *Int. J. Heat Mass Transfer*., vol. **70**, pp. 61–70, 2014.

[61] Vasu, B., Dubey, A., & Bég, O. A. (2019). "Finite element analysis of non-Newtonian magneto-hemodynamic flow conveying nanoparticles through a stenosed coronary artery". *Heat Transfer-Asian Research*, 49, 33-66.

[62] Elnaqeeb, T., Shah, N. A., & Mekheimer, K. S. (2019). "Hemodynamic characteristics of gold nanoparticle blood flow through a tapered stenosed vessel with variable nanofluid viscosity". *BioNanoScience*, 9(2), 245-255.

[63] Dubey, A., Vasu, B., Anwar Bég, O., Gorla, R. S., & Kadir, A. (2020). "Computational fluid dynamic simulation of two-fluid non-Newtonian nanohemodynamics through a diseased artery with a stenosis and aneurysm". *Computer Methods in Biomechanics and Biomedical Engineering*, 1-27.

[64] Zaman, A., Ali, N., & Khan, A. A. (2020). "Computational biomedical simulations of hybrid nanoparticles on unsteady blood hemodynamics in a stenotic artery". *Mathematics and Computers in Simulation*, 169, 117-132.

[65] V. R. Prasad, S. A. Gaffar and O. Anwar Bég, "Heat and mass transfer of a nanofluid from a horizontal cylinder to a micropolar fluid", *AIAA J. Thermophysics Heat Transfer,* 29, 1, 127-139 (2015).

[66] Nur Amalina Latiff, Md. Jashim Uddin, O. Anwar Bég and Ahmad Izani Md. Ismail, "Unsteady forced bioconvection slip flow of a micropolar nanofluid from a stretching/ shrinking sheet", *Proc. IMECHE- Part N: J. Nanoengineering and Nanosystems,* 230 (4) pp. 177–187 (2016).

[67] Tiwari RK, Das MK (2007) "Heat transfer augmentation in a two-sided lid-driven differentially heated square cavity utilizing nanofluids". *Int J Heat Mass Transfer* 50: 2002–2018.

[68] F. Hecht, '*FreeFem++*', 3rd Edition, Version 3.17, http://www.freefem.org/ff++ (2017).

[69] J. Happel and H. Brenner, "*Low Reynolds Number Hydrodynamics*", Prentice-Hall, New York, USA (1965).

[70] G.K. Batchelor, "The stress system in a suspension of force-free particles", *J. Fluid Mechanics*, 41 (3), 545-570 (1970).

[71] Y.C. Fung, "*Biomechanics: Motion, Flow, Stress and Growth*", Mac-Graw-Hill, New York, USA (1990).

[72] J. Mazumdar, "*Biofluid Mechanics*", World Scientific, Singapore (1992).